

Spatial and morphometric analysis of a comprehensive dataset of loess sinkholes from a small basin in the Chinese Loess Plateau

Sheng Hu^{1,2}, Francisco Gutiérrez³, Fanyu Zhang⁴, Sisi Li^{1,5}, Ninglian Wang^{1,2},

Xi-an Li⁶, Xingang Wang⁷, Jinhui Sun¹, Songbai Wu^{1,2}

¹ Shaanxi Key Laboratory of Earth Surface System and Environmental Carrying Capacity, College of Urban and Environmental Sciences, Northwest University, Xi'an 710127, China

² Institute of Earth Surface System and Hazards, Northwest University, Xi'an 710127, China

³ Departamento de Ciencias de la Tierra, Universidad de Zaragoza, C/ Pedro Cerbuna 12, 50009 Zaragoza, Spain

⁴ MOE Key Laboratory of Mechanics on Disaster and Environment in Western China, Department of Geological Engineering, Lanzhou University, Lanzhou 730000, China

⁵ School of Information Science and Technology, Northwest University, Xi'an 710127, China

⁶ School of Geological Engineering and Geomatics, Chang'an University, Xi'an 710054, China

⁷ State Key Laboratory of Continental Dynamics, Department of Geology, Northwest University, Xi'an 710069, China

Correspondence: Fanyu Zhang (zhangfy@lzu.edu.cn)

23 **Abstract.** From a global perspective, the basic mapping and investigation of the loess
24 sinkholes are far less extensive and in-depth than those of karst sinkholes. To some extent, this
25 has limited people's understanding of the morphological characteristics, development patterns,
26 and formation mechanisms of the loess sinkholes. The Chinese Loess Plateau (CLP) features
27 the most typical loess landforms in the world, where tens of thousands of loess sinkholes have
28 developed. However, due to the lack of high-precision and high-resolution survey data, the
29 identification, characterization, and quantification of sinkholes in the CLP are basically blank,
30 which significantly hinders in-depth research on loess sinkholes. In this study, we investigated
31 a typical watershed in the CLP using photogrammetry, airborne laser scanning, and a handheld
32 laser scanner. Based on previous studies, this paper introduces indices and methods for the
33 morphological quantification of loess sinkholes and constructs the first-ever dataset of loess
34 sinkhole morphology containing 1,194 records at the basin scale. On this basis, we completed
35 the spatial mapping of loess sinkholes, analysis of distribution patterns, morphological analysis,
36 size-frequency analysis, fitting analysis of different parameters, estimation of subsurface soil
37 erosion, in-depth investigation of typical sinkholes, and quantification of the contributions of
38 different factors to sinkhole development. These efforts provide rich information for a deeper
39 understanding of the morphological characteristics and genesis of loess sinkholes and offer data
40 support for comparative studies with sinkholes in other regions. More importantly, we
41 preliminarily estimate that the subsurface soil erosion triggered by sinkholes in the study area
42 reaches as high as 345,000 metric tons. This finding underscores that loess sinkholes are not
43 only a geological disaster but also a serious form of soil loss, highlighting their undeniable

44 significance in regional soil erosion studies and laying a solid foundation for subsequent
45 research and disaster prevention efforts. Furthermore, we suggest that the integration of
46 airborne laser scanning and handheld laser scanning may represent a new trend in the detailed
47 investigation of sinkholes in the future. This dataset is available on the Zenodo platform
48 (<https://doi.org/10.5281/zenodo.14000267>).

49 **1 Introduction**

50 It is widely recognized that soil erosion poses a global environmental problem with
51 significant socioeconomic implications (Morgan, 2005; Poesen, 2018; Llena et al., 2024). When
52 the term ‘soil erosion’ is mentioned, most people envision surface processes such as sheet, rill,
53 gully, or gravity erosion. However, subsurface mechanical erosion caused by soil piping and
54 the resulting surface collapse remains largely overlooked (Bernatek-Jakiel and Poesen, 2018).
55 The extensive international literature on soil erosion reveals a pronounced knowledge gap in
56 soil piping research. Soil piping involves the formation of shallow conduits in soils and weakly
57 consolidated sediments through seepage, pipe flow, and mass movements (e.g., wall and roof
58 collapse) (Bernatek-Jakiel and Poesen, 2018). Soil pipes, owing to their concealed nature and
59 complex patterns, are typically detected only after their collapse reaches the surface, forming a
60 sinkhole (Donnelly, 2008; Bernatek, 2015; Bernatek-Jakiel et al., 2017). Ground instability
61 resulting from sinkhole development poses threats to agriculture, transportation infrastructure,
62 water storage facilities, oil and gas pipelines, buildings, and other human assets and activities
63 (Gibbs, 1945; Gutiérrez et al., 2003, 2014; Richards and Reddy, 2007; Peng et al., 2018; Hu et
64 al., 2020). Piping sinkholes contribute to soil erosion and can trigger or exacerbate hazardous

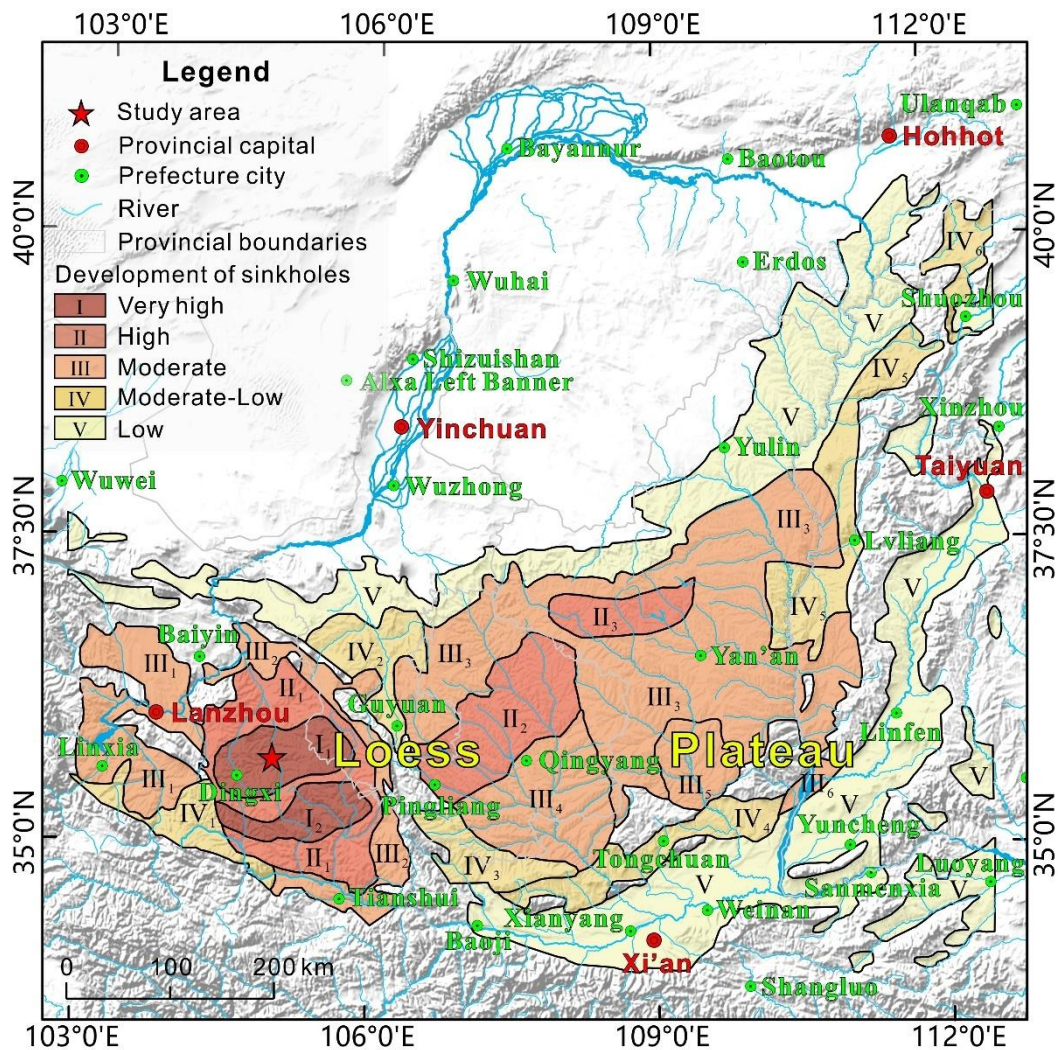
65 processes such as ground collapse, landsliding, debris flows, and gullyng (Peng et al., 2018; Li
66 et al., 2020; Hu et al., 2022; Wang et al., 2024). Therefore, gaining insight into the factors
67 controlling piping-related sinkholes, their morphometry, and spatial distribution patterns is of
68 paramount scientific and practical importance (Hofierka et al., 2018; Bernatek-Jakiel et al.,
69 2019).

70 The identification of sinkholes and the compilation of comprehensive sinkhole inventories
71 constitute a fundamental yet challenging task. In recent decades, several countries have
72 conducted extensive research on karst and piping sinkholes and developed national or regional
73 geodatabases (Gao et al., 2002, 2005; Farrant and Cooper, 2008; Rajabi, 2018; Vennari and
74 Parise, 2022; Hu et al., 2024). Traditional sinkhole mapping primarily relies on topographic
75 maps, digital elevation models (DEM), historical aerial photography, or satellite imagery
76 (Panno et al., 1997; Panno and Luman, 2013; De Carvalho Júnior et al., 2014; Vajedian and
77 Motagh, 2019; Gökkaya et al., 2021). However, the data collected through conventional
78 methods are often hampered by poor spatial resolution, making them inadequate for the
79 comprehensive and accurate mapping and morphometric characterization of soil sinkholes,
80 which are usually small. Consequently, researchers have increasingly turned to unmanned
81 aircraft systems (UAS) equipped with optical lenses, LiDAR sensors, and thermal cameras to
82 investigate piping sinkholes (Lee et al., 2016; Wu et al., 2016; Hofierka et al., 2018; Hu et al.,
83 2020; Li et al., 2024). UAS technology can capture imagery and topographic data with high
84 resolution and accuracy, and may even allow for vegetation filtering in the case of LiDAR data.
85 Despite the variety of techniques and approaches currently available, each still possesses

86 inherent limitations or shortcomings (Bernatek-Jakiel and Poesen, 2018). For instance, although
87 UAS-based photogrammetry can yield high-resolution topographic models, those models do
88 not allow for the reliable measurement of 3D morphometric parameters of piping sinkholes,
89 such as depth or volume (Li et al., 2024). Airborne LiDAR, while capable of partly penetrating
90 vegetation to reveal the underlying ground surface, typically employs orthogonal scanning,
91 thereby missing zones along the vertical walls of collapsed pipes, and consequently failing to
92 capture the complete inner morphology of the sinkholes (Jiang et al., 2024). The
93 aforementioned mapping technologies and methods are suitable for regional sinkhole surveys,
94 but they are inadequate for characterizing the internal morphology of individual sinkholes. In
95 recent years, handheld laser scanners based on simultaneous localization and mapping (SLAM)
96 technology have been developed and successfully applied to forest surveys, archaeological
97 studies, as well as tunnel and sinkhole investigations (Jones and Beck, 2017; Konsolaki et al.,
98 2020; Mokroš et al., 2021; Yuan et al., 2022; Hu et al., 2024; Jiang et al., 2024). When
99 conducting non-destructive identification and characterization of soil pipes and their associated
100 sinkholes, it is essential to select the most suitable investigation technique or to combine several
101 complementary methods, taking into account factors such as the characteristics of the target
102 features and the survey area (Bernatek-Jakiel and Kondracka, 2016; Borah et al., 2022).

103 A review on soil piping (Bernatek-Jakiel and Poesen, 2018) synthesizes current knowledge
104 globally and outlines directions for future research. By collating data from 230 documented
105 piping sites worldwide, the authors produced the first global map of soil-piping investigations,
106 demonstrating that piping erosion occurs across all climate zones and most soil types. However,

107 the review reveals a striking paucity of research on soil pipes in the Chinese Loess Plateau
108 (CLP), with only two documented study sites. It is widely recognized that the CLP, covering
109 64×10^4 km², hosts the world's most representative loess accumulation. Due to the relatively
110 high permeability, collapsibility, and water sensitivity of loess deposits, together with their
111 porous and jointed structure, pipes and sinkholes can readily form under the presence of water
112 (Li et al., 2010; Geng et al., 2023; Zhang et al., 2026). In recent years, some scholars in China
113 have recognized loess sinkholes as a specific geological hazard and have called for increased
114 attention and research on this process given its growing economic implications (Li et al., 2010,
115 2020; Peng et al., 2018). The intensity map of sinkhole development in the CLP (Fig. 1) shows
116 that the western region exhibits a higher intensity of sinkhole development compared to the east,
117 particularly in the Dingxi and Huining areas, where sinkhole densities typically reach 243 and
118 265 sinkholes per km², respectively (polygon I₁ in Figure 1) (Peng et al., 2018; Hu et al., 2020).
119 Notably, no regional morphometric datasets of piping sinkholes have yet been published,
120 constraining our understanding of their morphological characteristics and developmental
121 patterns.



122
 123 **Figure 1.** Map illustrating the degree of piping-related sinkhole development in the Chinese
 124 Loess Plateau, grouped into five categories (Peng et al., 2018; Hu et al., 2020). The star
 125 denotes the location of the study area within a zone of very high sinkhole development.

126 In view of the above, the principal objectives of this study are:

127 (i) to perform a comprehensive and high-resolution survey of loess sinkholes in a
 128 representative basin of the CLP by integrating UAS photogrammetry, airborne LiDAR, and a
 129 SLAM-based handheld laser scanner (HLS);

130 (ii) to characterize the morphometric features of the sinkholes and produce an open-access
 131 database comprising 1194 sinkhole records, supplemented with data on multiple attributes;

132 (iii) to analyze the spatial distribution patterns of the sinkholes and their relationships with
133 other landforms in order to gain insight into the main controlling factors;

134 (iv) to conduct an in-situ investigation inside a typical sinkhole using the HLS, evaluating
135 the potential and advantages of SLAM technology for complete sinkhole characterization.

136 Through these efforts, we aim to partially fill the current knowledge gap on loess sinkholes
137 in the CLP and identify suitable surveying approaches. This will make available a unique case-
138 study dataset to the global soil-piping community and will provide a scientific basis for
139 assessing and managing sinkhole risk in the region. The presented results reveal the strikingly
140 large subsurface erosion volume attributable to piping erosion, underscoring that soil-piping
141 research merits intensified attention, rather than continued neglect.

142 **2 Study area**

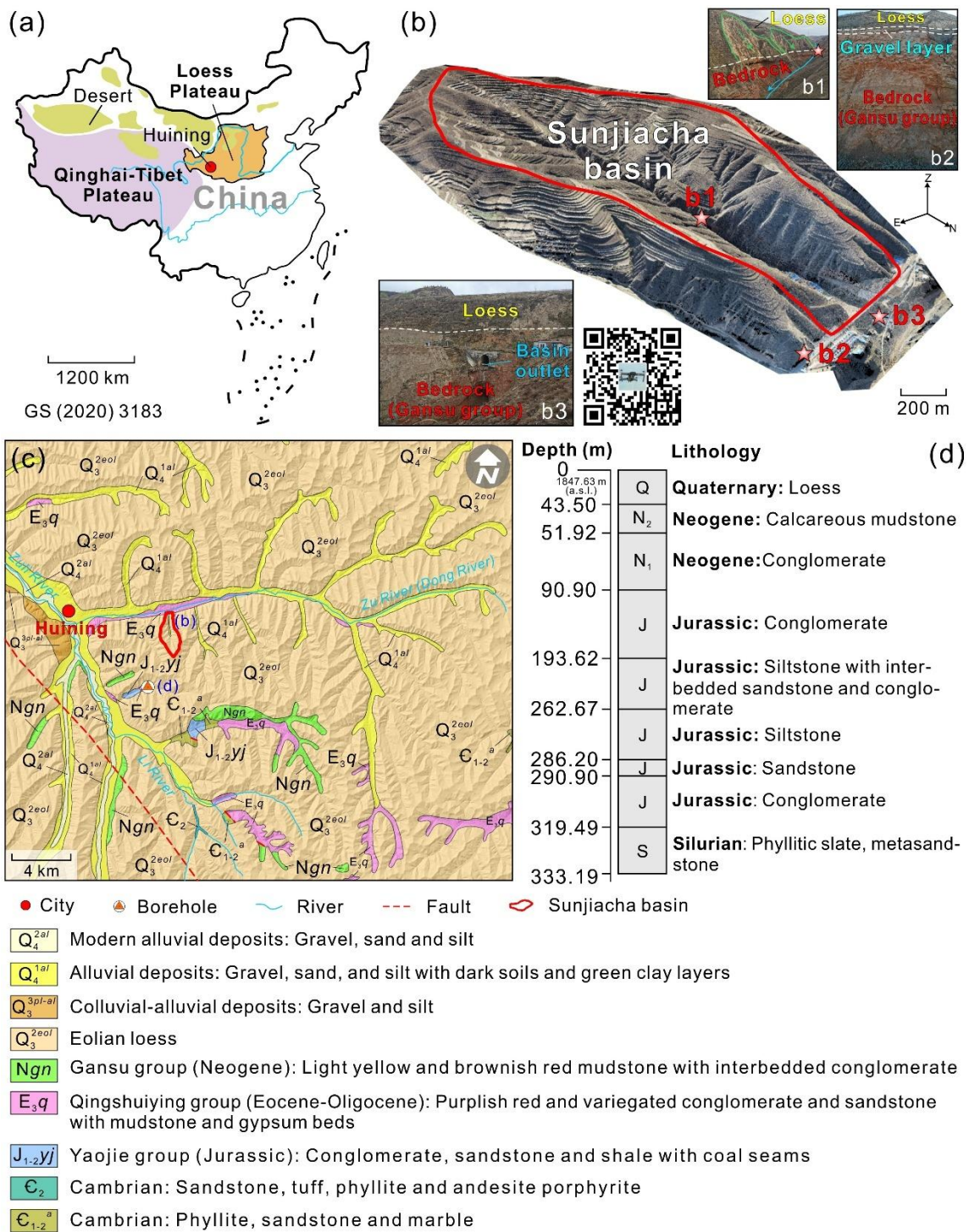
143 The study area is a small leaf-shaped watershed drained by the N-flowing Sunjiacha stream.
144 It is located in the southwestern sector of the Loess Plateau of China, approximately 5 km east
145 of Huining city (Figs. 2a-c). The drainage basin is approximately 2960 m long, and 1280 m
146 wide, covering about 2.4 km², and is characterized by sparse grassland vegetation. The
147 elevation ranges from 2070 m a.s.l. (highest point of the divide) to 1724 m a.s.l. (outlet),
148 resulting in a local relief of 346 m. The region is characterized by a semi-arid temperate
149 monsoon climate, with a mean annual precipitation of 370 mm. Much of the rainfall occurs
150 between May and September, and frequent severe rainfall events can account for up to 96% of
151 the monthly precipitation (Hu et al., 2020). Sunjiacha stream is an ephemeral channel that
152 carries water flow after storms or rainy periods. Most of the slopes in the basin, with the

153 exception of some sectors in the lower part, have been transformed into a terraced landscape on
154 loess deposits for cultivation and erosion control (Fig. 2b).

155 From a geological perspective, the investigated zone is located in the Longxi Basin. Its
156 development began during the Yanshan orogeny (ca. 205~66 Ma), continued further during the
157 Himalayan orogeny (ca. 50 Ma to present), and finally took shape as the Longxi graben basin
158 by the late Neogene. The basement of the basin is composed of Proterozoic metamorphic rocks,
159 Paleozoic volcano-sedimentary rocks, Caledonian intrusive rocks and Mesozoic-Cenozoic
160 sedimentary successions. Since the end of Neogene to the Quaternary, the Longxi Basin has
161 been uplifted together with the Qinghai-Tibet Plateau and its surrounding mountains (Niu,
162 2023). The tectonic uplift in the Quaternary has been accompanied by (Figs. 2b, c): (1)
163 downcutting of the drainage network into the Neogene sediments of the Gansu group; and (2)
164 accumulation of loess and terraces over the relatively flat Gansu group red beds, forming a thick
165 loess-paleosoil succession. The 1:200,000 scale regional geological map indicates that most
166 slopes in the area are underlain by the Q₃ aeolian loess (Malan loess), while Q₄ alluvial and
167 colluvial deposits, largely derived from the former, are mainly found in the valley floors (Fig.
168 2c). Fig. 2d shows a simplified log of the 333 m deep Huining #11 borehole drilled 2.6 km
169 south of the Sunjiacha basin by the China Geological Survey in 1972, revealing a Quaternary
170 loess thickness of 43.5 m. In the 1960s, Liu (1964, 1965) observed a gradual NW-to-SE grain-
171 size decrease in the loess across the CLP, and divided it into three zones: sand loess, typical
172 loess, and clayey loess. This spatial pattern is attributed to factors such as the distance from the
173 source area and the southeastward weakening of winds in winter (Yang and Ding, 2017).

174 Previous studies have shown that the Huining loess contains both dust from inland desert areas
175 and detritus generated during the Pleistocene glaciations on the Qinghai-Tibet Plateau (Peng,
176 2014). Because Huining is close to both source regions, relatively coarse sand and silt particles
177 were deposited here by the northwesterly winds. Thus, the large pore size characteristic of the
178 Q₃ Malan loess is particularly pronounced in this area. The Q₃ Malan loess is a light grey-yellow
179 silt-dominated deposit with relatively uniform particle distribution, loose granular texture and
180 blocky morphology. The grain size of the loess-paleosol sequence at Duanxian site (S0~L29;
181 62 km north of our study area) studied by Niu (2023) is generally coarse, with a median particle
182 size ranging from 12 to 38.8 μm (silt size range: 2~50 μm). Particles >32 μm and >63 μm
183 represent around 60% and 25% of the silt-dominated deposit, respectively (Niu, 2023).

184 The thickness of the Q₃ Malan loess is highly variable, ranging from several meters to tens
185 of meters. Under the presence of infiltration water, the Q₃ Malan loess, which is often affected
186 by vertical joints, is highly susceptible to hydrocompaction and piping, giving rise to unique
187 loess sinkhole landscapes. In fact, this area is widely recognized as having the highest density
188 of loess sinkholes in the vast Loess Plateau, covering 6370 km² (2.33% of the loess
189 accumulation in China) (Fig. 1). The average density of sinkholes in our study area is ca. 500
190 sinkholes/km². The investigated drainage basin, characterized by a dendritic gully network and
191 terraced slopes, displays a large number of loess-related ground instability features, including
192 1194 loess collapse sinkholes and 288 landslides (Fig. 3). The latter include slope movements
193 with deep and shallow sliding surfaces, typically induced by fluvial undercutting, artificial
194 excavations, and intense rainfall events.



195

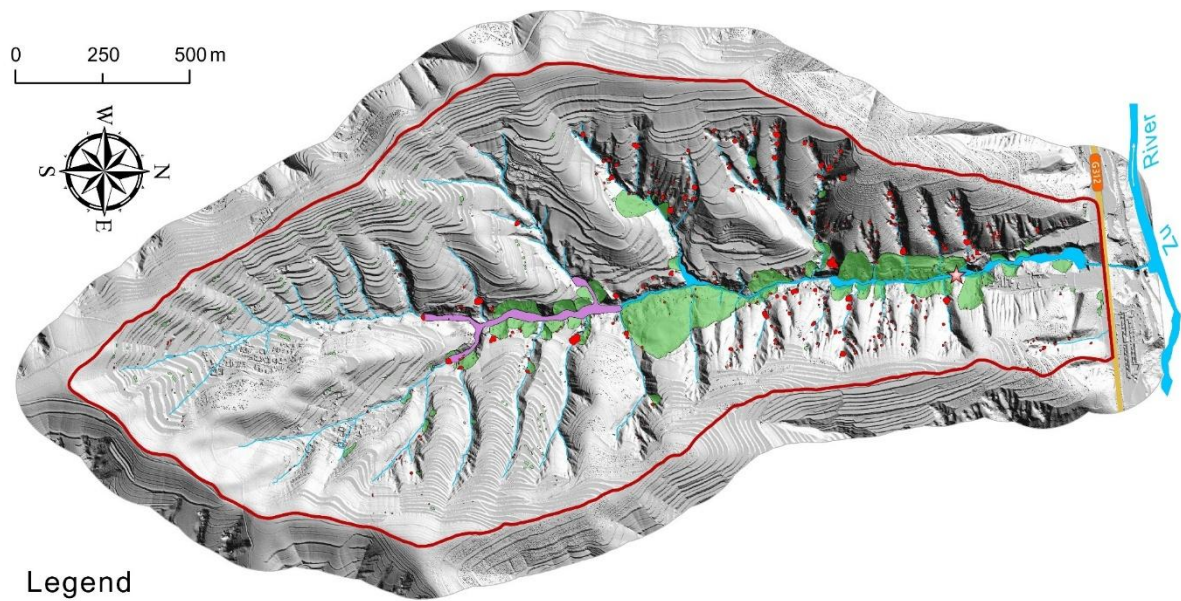
196 **Figure 2.** Geographic and geological setting of the Sunjiacha drainage basin within the Loess

197 Plateau: (a) Location of the study area; (b) 3D model of the Sunjiacha basin generated by

198 Structure from Motion Photogrammetry with UAS images. The QR code provides access

199 (<https://www.720yun.com/t/0cvktq7yg2w>) to an online panorama of the study area created

200 with drone images; (c) 1:200,000 scale regional geological map (data source: available at
201 <http://dcc.ngac.org.cn/>); (d) Stratigraphic log of the Huining #11 borehole drilled for coal
202 exploration 2.6 km south of the study area (see location in c) (data source: available at
203 <http://zk.cgsi.cn/>).



Legend

● Sinkholes (n=1194) ▲ Landslides (n=288) ▬ Landslide-dam deposits 🛣️ National highway
 🗺️ Water divide 🌊 Main channel 🌊 Tributary 🛣️ Highway culvert 🏞️ Terrace ★ Knickpoint

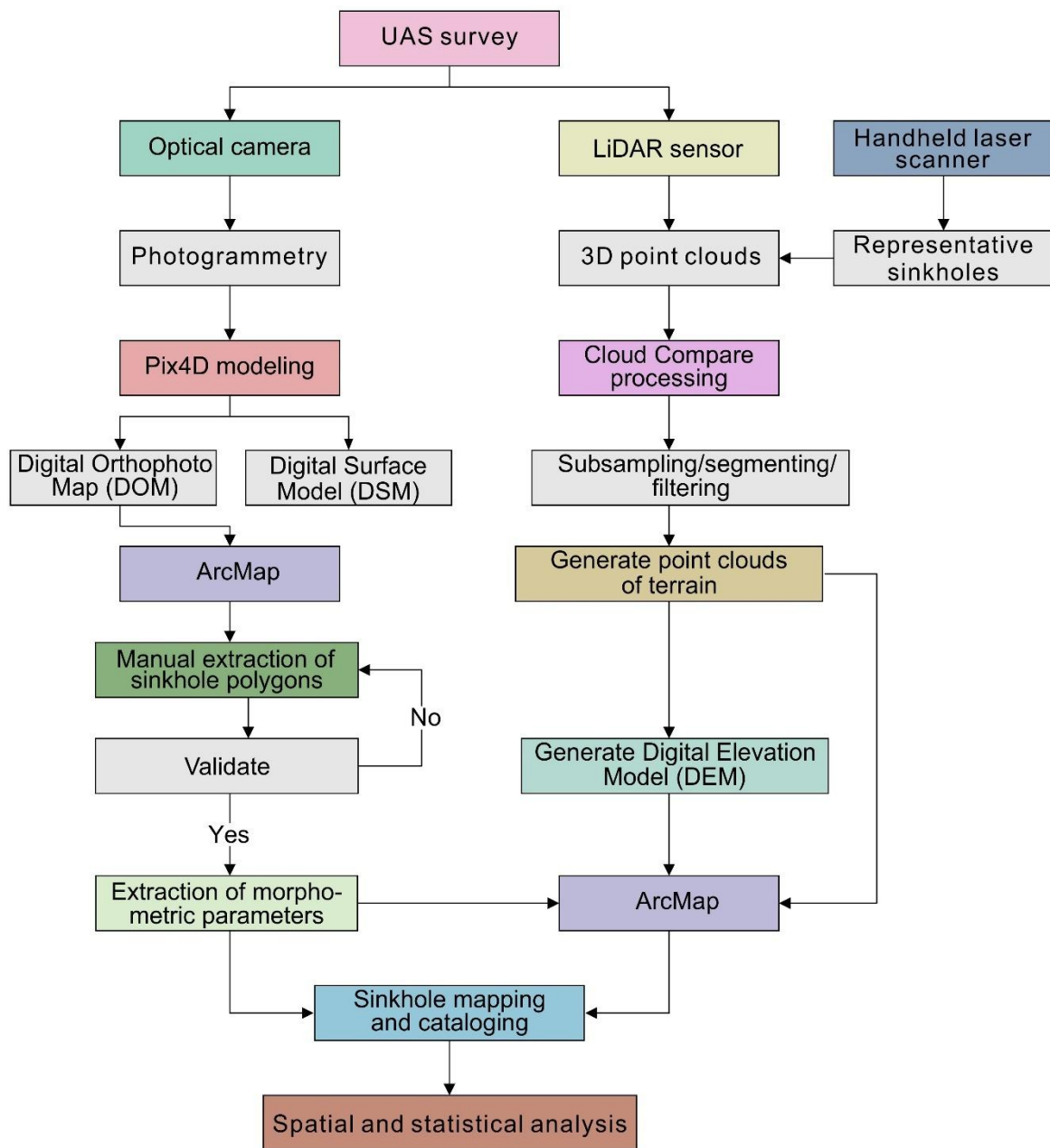
Figure 3. Geomorphological map illustrating the distribution of loess sinkholes, landslides, and deposits accumulated upstream of a landslide dam in the Sunjiacha basin.

3 Methods

3.1 Technical procedure

The flow diagram in **Figure 4** outlines the data acquisition and analysis approach adopted in this investigation, which consisted of several key steps. Initially, we performed surveys using an unmanned aircraft system (UAS) equipped with optical cameras and LiDAR sensors, along with a handheld laser scanner (HLS). Subsequently, the data collected during these surveys enabled the generation of a Digital Orthophoto Map (DOM), a bare-surface Digital Surface Model (DSM), a Digital Elevation Model (DEM), and 3D terrain point clouds. The drone imagery was processed with the Structure from Motion photogrammetry software Pix4D Mapper v4.5.6 (<https://www.pix4d.com/>), while the open-source Cloud Compare v2.13.2 software (<http://www.cloudcompare.org/>) was used to analyze the point clouds. ArcMap 10.5

218 was used to manually map the sinkholes and extract planimetric and three-dimensional
219 morphometric parameters from the DOM, DEM and relief maps. This enabled the creation of a
220 cartographic sinkhole inventory containing a number of categorical and numerical attributes for
221 the morphometric and statistical analysis of the sinkholes. 3D data of the loess sinkholes, such
222 as elevation and depth, were derived from noise-filtered terrain point clouds acquired with
223 airborne LiDAR, rather than directly from the UAS-derived DSM, which significantly
224 enhanced the accuracy of the parameters.



225

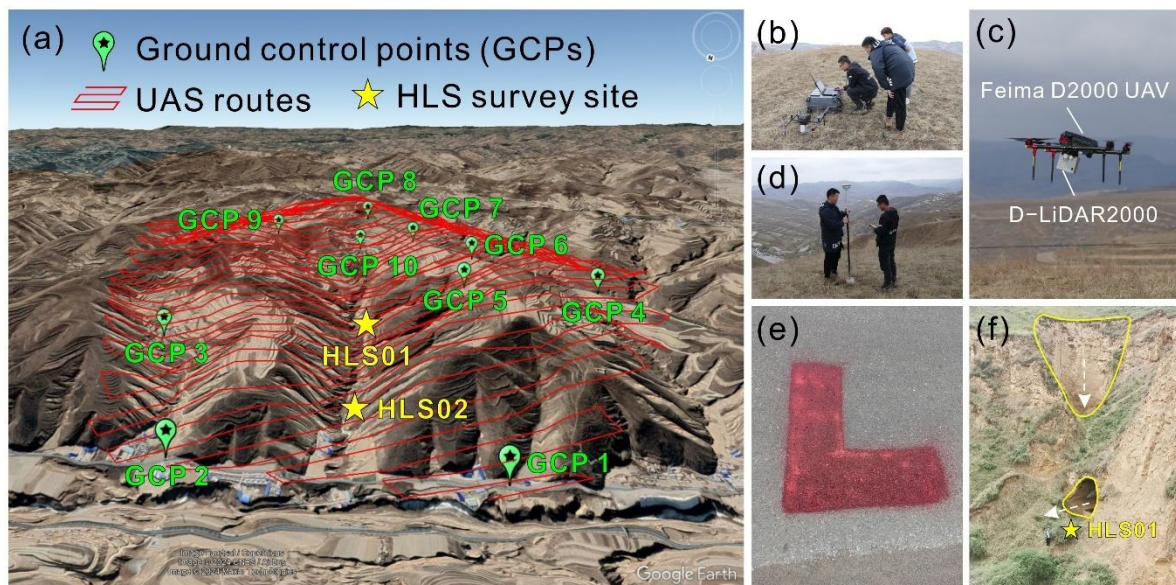
226 **Figure 4.** Flow chart outlining the data collection, processing, and analysis approaches.

227 **3.2 Field investigations**

228 **3.2.1 UAS survey**

229 On April 9, 2021, we engaged the professional company Feima Robotics to conduct a
 230 detailed survey of the research area using a D2000 UAS (Figs. 5a-e). We carried out two flight
 231 missions at a height of 200 m utilizing the D-Lidar 2000 LiDAR sensor (linear scanning) and

232 the D-CAM2000 optical camera mounted on the drone. Images were taken with longitudinal
 233 and lateral overlaps of 70% and 60%, respectively. Point clouds were acquired with a lateral
 234 overlap of 40%. A total of 11 ground control points (GCPs) were distributed across the area and
 235 measured with a DGPS. Detailed specifications of the UAS and its sensors are available at
 236 <http://www.feimarobotics.com/zhcn/productDetailD2000>. The D-Lidar 2000 module employs
 237 three-echo technology, which ensures effective penetration through vegetation to obtain more
 238 accurate bare-ground data. After completing the field survey, we pre-processed the collected
 239 data with the UAV Manager v1.7.0 software to produce a 3 cm resolution Digital Orthophoto
 240 Map (DOM) and a Digital Surface Model (DSM), along with raw point cloud data (40 GB;
 241 average density of 192 points/m²). The modeling report from UAV Manager indicated that the
 242 average RMSE (root-mean-square error) for the 11 ground control points (GCPs) was 0.0137
 243 m, with RMSEs of 0.012 m, 0.014 m, and 0.015 m for the X, Y, and Z coordinates, respectively.
 244 An elevation accuracy assessment of 19 laser point cloud validation points measured with the
 245 DGPS revealed an average RMSE of 0.029 m, with a maximum error of 0.058 m.



246

247 **Figure 5.** Surveying of the study area with an UAS (Li et al., 2024) and a handheld laser
248 scanner: (a) Terrain model of the study area draped by a Google Earth image. Red lines depict
249 the UAS flight paths. Green paddle icons show the distribution of ground control points
250 (GCPs) used to improve the accuracy of the UAS models. Yellow stars indicate the location of
251 the handheld laser scanner surveys; (b-e) Unmanned aerial system field operations with the
252 control unit (b), the drone (c), a DGPS (d) and GCPs (e); (f) Using the GeoSLAM (ZEB
253 Horizon) handheld laser scanner to scan the interior of a sinkhole in a steep slope with an
254 opening at the bottom.

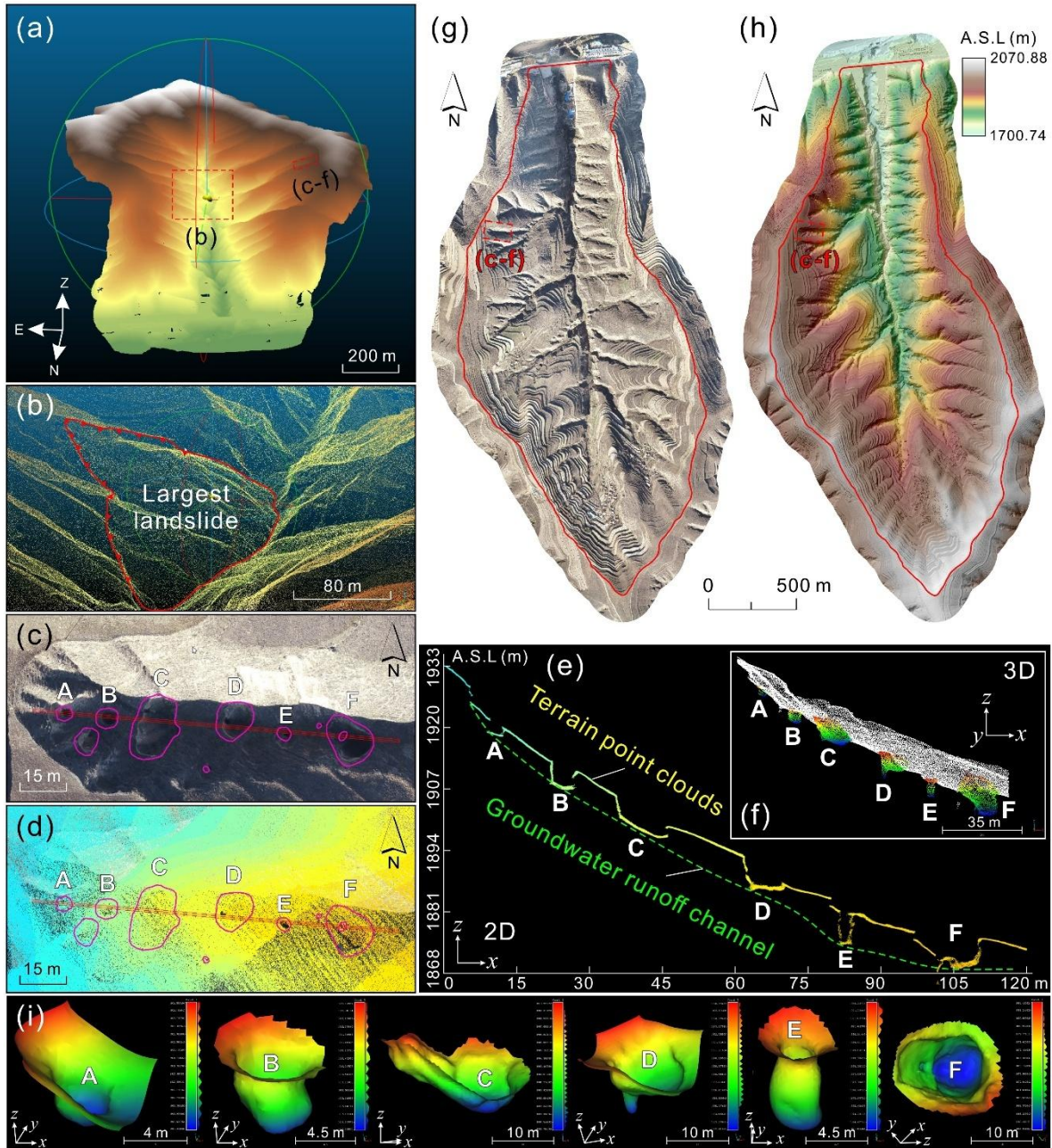
255 *3.2.2 Handheld laser scanner survey*

256 We used a GeoSLAM ZEB Horizon handheld LiDAR scanner (<https://geoslam.com/>) with
257 a maximum range of 100 m to carry out high-resolution scans of thirteen representative
258 sinkholes (1 sinkhole at HLS01 site; 12 sinkholes at HLS02 site; see location in **Figures 5a, f**).
259 This device utilizes SLAM (Simultaneous Localization and Mapping) technology, enabling
260 real-time recording of point cloud data of the terrain or objects with accurate geographic
261 coordinates. It weighs 1.45 kg, and records 300,000 points per second with a measurement error
262 ranging from 6 mm to 30 mm. After the field survey, we pre-processed and post-processed the
263 point cloud data using GeoSLAM Draw v4.0 and Cloud Compare software v2.13.2, and
264 subsequently we obtained noise-filtered terrain point clouds and DEMs of the representative
265 sinkholes.

266 *3.2.3 Surveying and mapping*

267 **Figure 6** shows some of the products derived from the UAS survey. We filtered the raw
268 point clouds using the Cloth Simulation Filter (CSF) developed by Zhang et al. (2016) in Cloud
269 Compare v2.13.2. The main parameter settings were: General parameter setting – check Steep

270 slope and Slope processing options; Advanced parameter setting – Cloth resolution 0.5 m,
271 Maximum iterations 999, Classification threshold 0.1 m. **Figure 6a** shows the terrain point cloud
272 processed in Cloud Compare v2.13.2 with above-surface noise removed (e.g., buildings, people,
273 vehicles, vegetation, towers, and power lines). **Figures 6b-f** show enlarged views of the dashed
274 boxes indicated in **Figures 6a, g-h**. **Figure 6b** illustrates the largest landslide in the study area.
275 **Figures 6c** and **6d** depict an orthoimage and a terrain point cloud of a gully with a string of
276 sinkholes related to a subsurface conduit created by internal erosion. **Figures 6e** and **6f** display
277 the 2D profile of the terrain point cloud and an excerpt of the 3D point cloud of a gully with
278 numerous sinkholes, respectively. **Figure 6g** shows the 6.87 cm resolution Digital Orthophoto
279 Map (DOM) derived from the drone images. **Figure 6h** presents the 0.5 m resolution Digital
280 Elevation Model (DEM) generated from the terrain point cloud data in **Figure 6a**. **Figure 6i**
281 depicts the 3D models generated by Poisson Surface Reconstruction in Cloud Compare v2.13.2,
282 based on LiDAR point-cloud data from six sinkholes. These spatial data provide the basis for
283 mapping and cataloging sinkholes, identifying sediment-discharge holes, and extracting
284 morphometric parameters.



285
 286 **Figure 6.** Results of the UAS survey: (a) Bare-surface point cloud of the study area after
 287 filtering out above-surface objects; (b-f) Enlarged views of the areas indicated by dashed
 288 boxes in a; (b) The largest landslide in the study area; (c-e) Orthoimage, point cloud, and a
 289 point-cloud section of a row of loess sinkholes (purple line in d) within a collapsed gully,
 290 respectively; (f) 3D perspective view of the area shown in d; (g) Digital orthophoto map
 291 (DOM) generated from images acquired during the UAS survey; (h) Digital elevation model
 292 (DEM) derived from the bare-surface point clouds; (i) Poisson surface reconstruction of
 293 sinkholes A-F as seen in f.

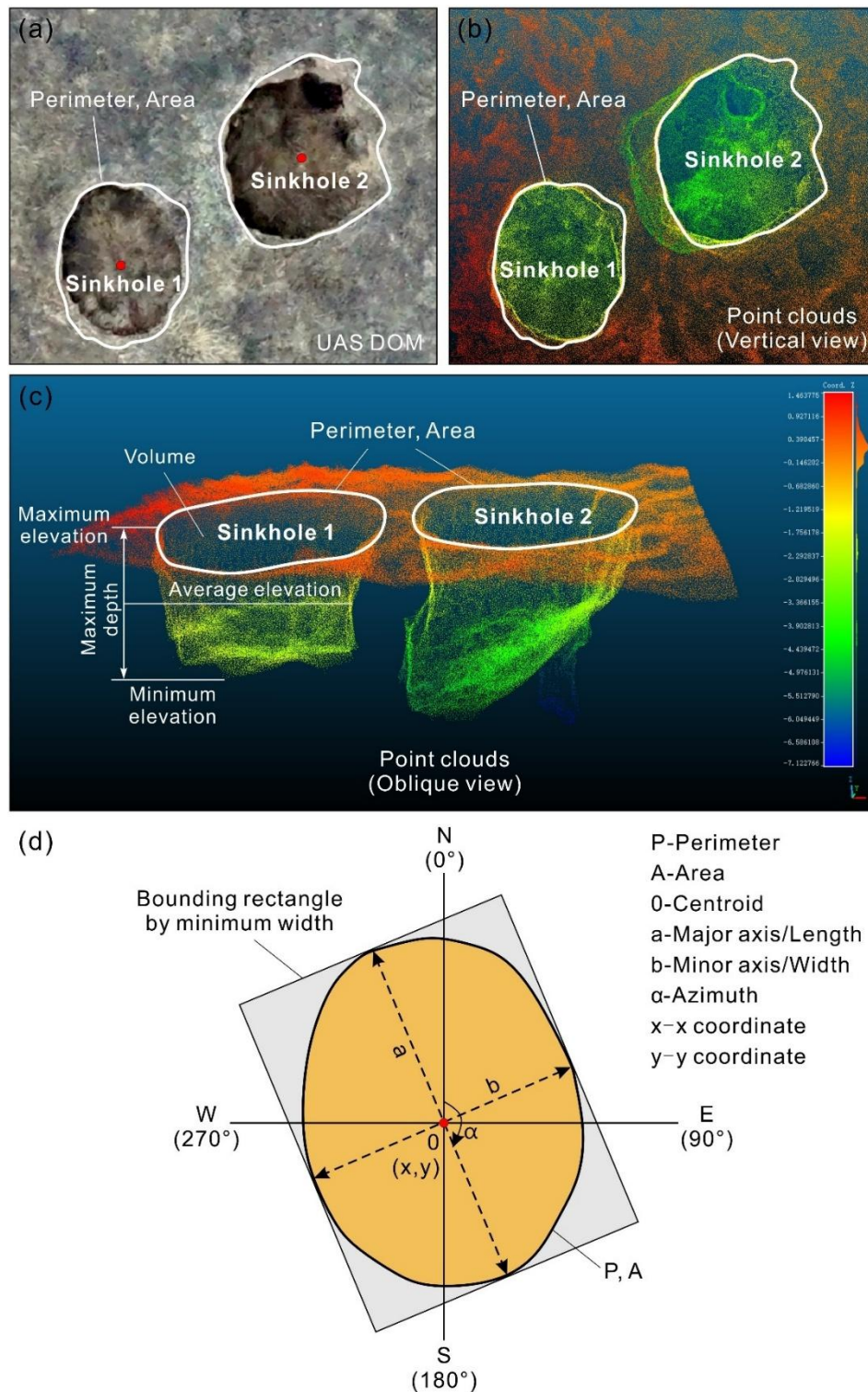
294 **3.3 Basic morphometric parameters and extraction methods**

295 Drawing on a literature review on studies about loess sinkholes and karst dolines
296 worldwide, we selected a number of morphometric parameters for the geometrical
297 characterization of the loess sinkholes (e.g., Day, 1983; Liu and Wang, 2008; De Waele and
298 Gutiérrez, 2022 and references therein). Table 1 presents the selected parameters, their
299 definitions, and the approach used for their automatic computation. The key morphological
300 parameters and their definitions are illustrated in Figure 7.

301 **Table 1** Morphometric parameters used for the characterization of loess sinkholes: index,
 302 definition and computing method.

Parameter	Unit	Computing method	Explanation	Reference
Coordinates	°	Calculate geometry in ArcMap attribute table	X, Y coordinates of the centroid of the sinkhole polygon	
Length (<i>L</i>)	m	Length of the fitted minimum bounding rectangle	Length of the major axis, given by the planimetric distance between the antipodal points of the perimeter	Kobal et al, 2015; Wu et al, 2016
Width (<i>W</i>)	m	Width of the fitted minimum bounding rectangle	Width perpendicular to major axis, given by the width of the fitted minimum bounding rectangle	Kobal et al, 2015; Wu et al, 2016
Azimuth (<i>Azi</i>)	°	ArcMap Minimum Bounding Geometry tool	Clockwise angle between the North and the major axis	Bruno et al, 2008; Kobal et al, 2015; Öztürk et al, 2018
Maximum elevation (<i>E_{max}</i>)	m	Extracted from point cloud data	Maximum elevation of the sinkhole perimeter	
Minimum elevation (<i>E_{min}</i>)	m	using LAS Point Statistics by Area tool in ArcMap	Minimum elevation at the sinkhole bottom	
Average elevation (<i>E_{ave}</i>)	m		Average elevation of the 3D points that define the sinkhole depression	
Maximum depth (<i>D_{max}</i>)	m	Extracted from point cloud data	Maximum elevation minus minimum elevation	De Waele and Gutiérrez, 2022; Sevil and Gutiérrez, 2023
Perimeter (<i>P</i>)	m	Calculate geometry in ArcMap attribute table	Planimetric length of the mapped edge of the sinkhole	Liu and Wang, 2008
Area (<i>A</i>)	m ²	Calculate geometry in ArcMap attribute table	Planimetric area enclosed by the perimeter	Liu and Wang, 2008
Volume (<i>V</i>)	m ³	$V=A \times D_{max}$	Volume of the 3D space corresponding to the sinkhole depression	Gökkaya et al., 2021; De Waele and Gutiérrez,

Elongation ratio (<i>ER</i>)	$ER=L/W$ or $ER=a/b$, where L (or a) and W (or b) are the major and minor axes (length and width) of the sinkhole, respectively	Length to width ratio	Day, 1983; Basso et al., 2013; Zumpano et al., 2019
Circularity index (<i>CLI</i>)	$CLI = 4\pi A/P^2$	Ratio between the area of the sinkhole and the area of a theoretical sinkhole having a circumference equal to the perimeter of the actual sinkhole. The lower the value below 1, the further to a perfect circular shape	De Carvalho Júnior et al., 2014
Compactness index (<i>COI</i>)	$COI = A/A_c$, where A_c is the area of the smallest circle circumscribing the sinkhole perimeter	Quantifies how much the shape of the sinkhole perimeter is close to a circle. The lower the value below 1, the more complex the sinkhole perimeter	Cole, 1964; Kim and Anderson, 1984; Li et al., 2013; Zhu and Pierskalla, 2016
Length to Depth ratio (<i>LDr</i>)	$LDr=L/D_{max}$	Ratio between sinkhole length and depth	Day, 1983



304

305 **Figure 7.** Diagrams illustrating the key morphometric parameters of the loess sinkholes: (a)

306 Orthoimage of sinkholes; (b) Vertical view of sinkholes point clouds (located at HLS 02 in

307 **Figure 5a**); (c) Oblique view of sinkholes point clouds; (d) Schematic diagram of key

308

morphometric parameters of sinkholes.

309 **4 Results**

310 **4.1 Sinkhole mapping and inventorying**

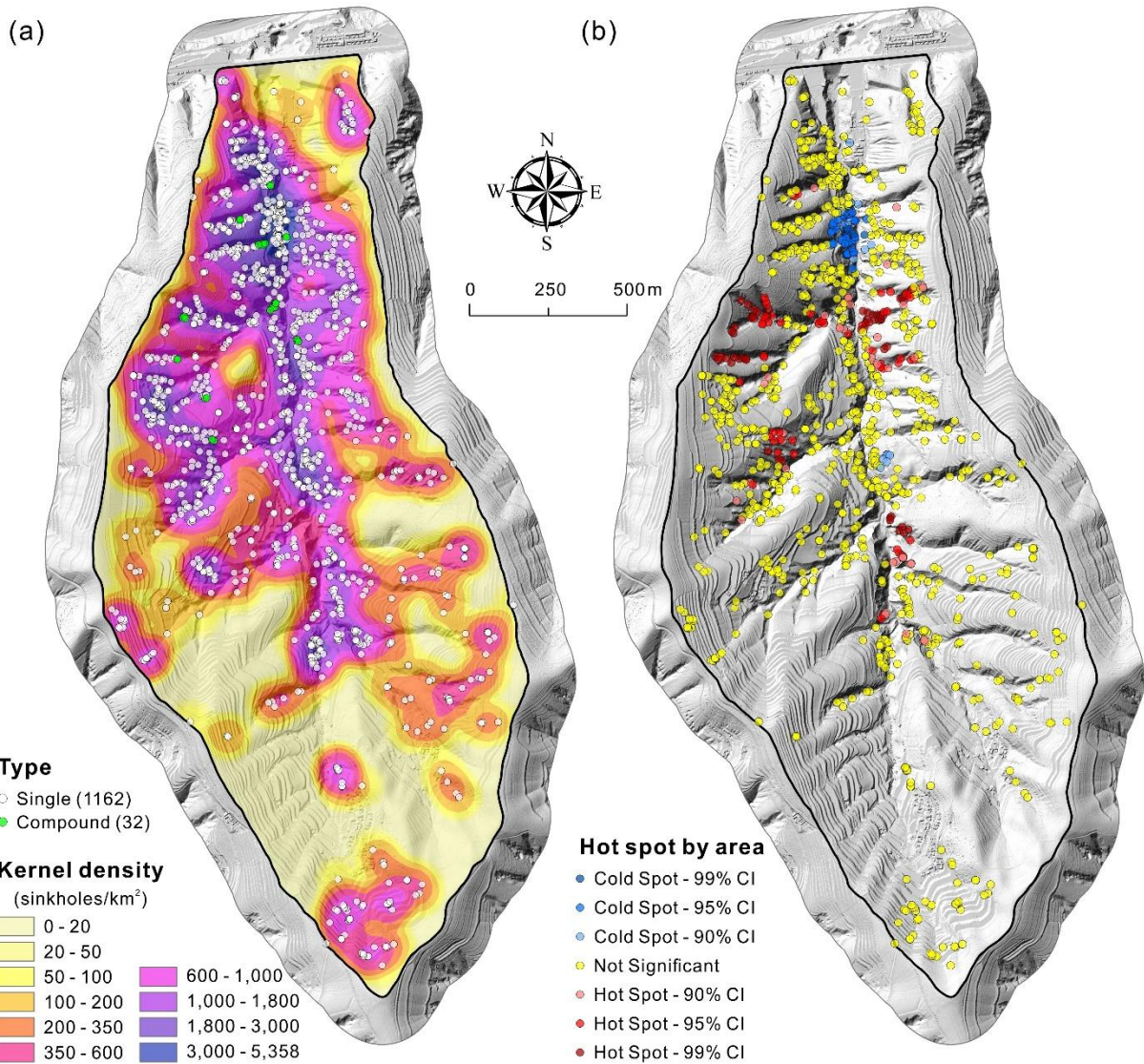
311 Given the exceptionally high-resolution of the data used for mapping, the inventory can
312 be considered nearly complete, even including small decimeter-scale holes. This information
313 furnished a database of 1194 loess sinkholes in the study area, each characterized by multiple
314 attributes (**Table 1** and **Data availability**): topographic (coordinates, azimuth, maximum,
315 minimum and average elevation); morphometric (length, width, depth, perimeter, area, volume,
316 geometrical indexes); and geomorphic (soil loss). The inventory also differentiates 1162 single
317 sinkholes, and 32 compound sinkholes resulting from the aggregation of two or more adjacent
318 sinkholes. This comprehensive database serves as the basis for the morphometric-statistical
319 analysis presented in this work. For the detailed cataloging and the statistical parameters of
320 these sinkholes, please refer to **Table 2** and **Data availability**. Additionally, 9 thematic maps
321 were generated with some parameters (length, maximum depth, perimeter, area, volume,
322 elongation ratio, circularity index, compactness index, length to depth ratio) to explore spatial
323 patterns of different value ranges. **Table 2** presents the main statistics of the sinkholes grouped
324 into three categories: all, single, and compound.

Table 2 Summary statistics of morphometric parameters for different types of sinkholes.

Statistical indicators	All sinkholes (1194)	Single sinkholes (1162)	Compound sinkholes (32)
Length (m)			
Range	0.19~35.11	0.19~35.11	0.88~33.9
Mean	3.75	3.65	7.37
Median	2.28	2.26	3.69
Depth (m)			
Range	0.42~29.60	0.42~29.60	2.05~18.50
Mean	6.55	6.48	8.36
Median	5.30	5.214	7.76
Perimeter (m)			
Range	0.60~104.14	0.60~98.92	2.67~104.14
Mean	10.75	10.45	21.51
Median	6.43	6.40	10.47
Area (m²)			
Range	0.03~662.18	0.03~662.18	0.50~635.75
Mean	17.75	16.42	66.19
Median	2.94	2.93	7.97
Volume (m³)			
Range	0.21~19601.27	0.21~19601.27	2.66~8405.93
Mean	334.75	310.79	1002.98
Median	42.78	42.10	81.28
Elongation ratio			
Range	1~4.55	1~4.55	1.04~1.98
Mean	1.37	1.37	1.31
Median	1.30	1.30	1.28
Circularity index			
Range	0.33~0.98	0.33~0.98	0.74~0.96
Mean	0.89	0.89	0.88
Median	0.92	0.92	0.90
Compactness index			
Range	0.45~0.88	0.45~0.88	0.70~0.82
Mean	0.78	0.78	0.77
Median	0.78	0.78	0.76
Length to depth ratio			
Range	0.11~6.06	0.11~6.06	0.30~2.56
Mean	0.84	0.87	0.87
Median	0.77	0.77	0.72

327 4.2 Spatial distribution patterns

328 The spatial distribution patterns of the loess sinkholes were analyzed considering their
329 relationships with other geomorphic features (Fig. 3) and using spatial analysis and statistics
330 tools (Fig. 8). The detailed geomorphological map of the Sunjiacha basin reveals that sinkholes
331 are preferentially distributed in the following zones (Fig. 3): (1) the margins of the deeply
332 entrenched lower-middle section of the Sunjiacha trunk stream; (2) tributary gully systems in
333 the lower-middle part of the Sunjiacha basin; (3) landslides (slid mass and crown), mostly
334 associated with the trunk channel; and (4) man-made terraces. The kernel density model in
335 Figure 8a shows low densities mainly associated with upper part of the Sunjiacha basin, where
336 the drainage network shows a lower degree of incision, and rounded divides characterized by
337 low local gradients. Overall, there is a good spatial correlation between sinkholes and areas
338 with high local topographic gradients and loess deposits disturbed by landslides. The hot spot
339 model based on sinkhole area shown in Figure 8b illustrates a pronounced cluster of small
340 sinkholes (cold spots in blue) associated with recent landslides in the lower sector of the basin.
341 Clustering of large sinkholes (hot spots in red) mainly occur along the main drainages of
342 tributary catchments in the lower part of the Sunjiacha basin.

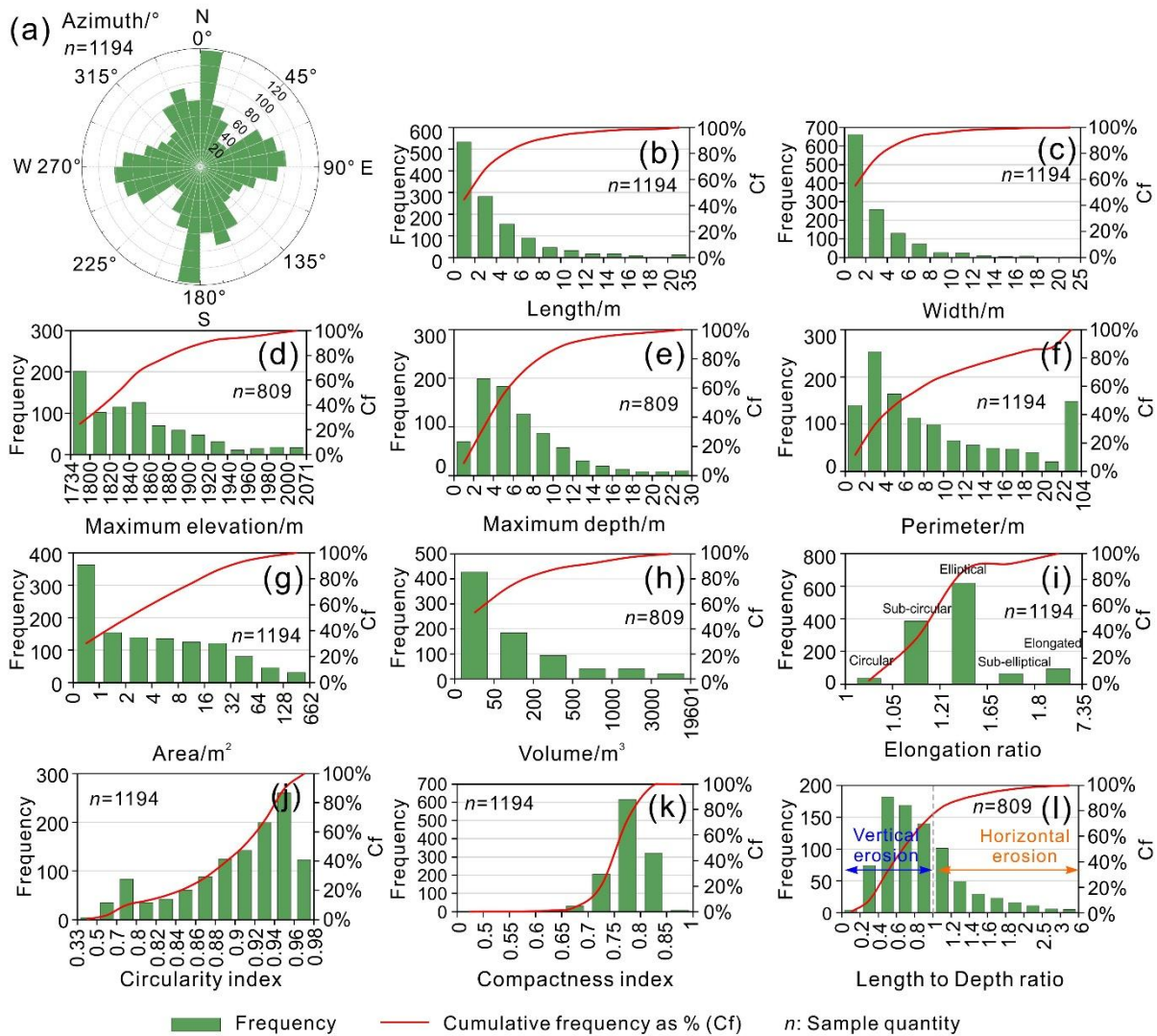


343
344 **Figure 8.** Spatial distribution patterns of loess sinkholes: (a) Sinkhole type and kernel density
345 map (search radius: 100 m); (b) Hot spot map by sinkhole area (threshold distance: 100 m).

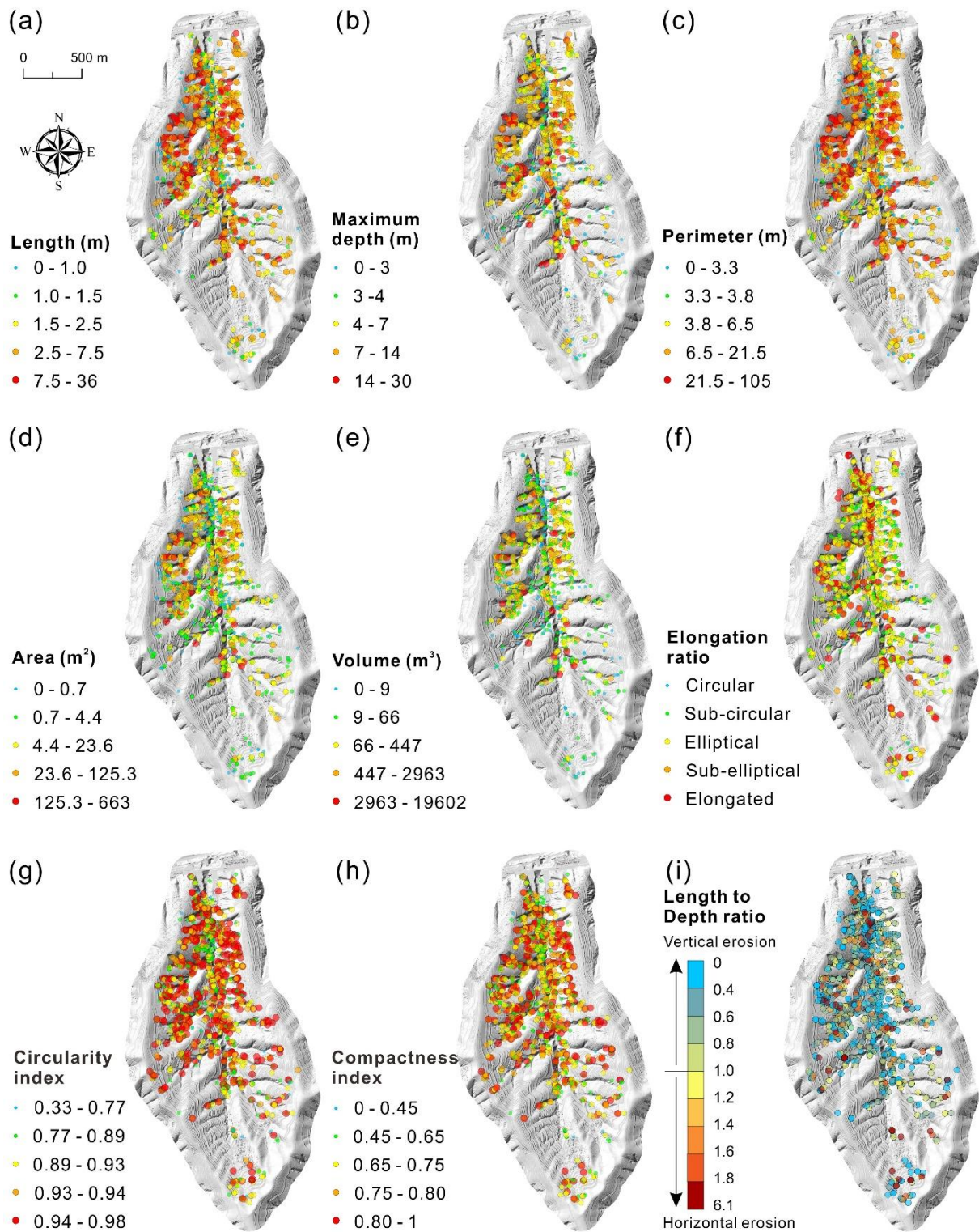
346 **4.3 Morphometric analysis**

347 In this section, we analyze the spatial and morphometric parameters computed for the 1194
348 inventoried sinkholes (1162 single, 32 compound), their frequency-size distribution (Fig. 9), as
349 well as some spatial patterns based on the distribution of different value ranges (Fig. 10). It
350 should be noted that the airborne LiDAR returned sparse and limited point clouds when
351 detecting sinkholes with diameters less than 1 m. Consequently, for the calculation of

352 parameters related to sinkhole depth and volume (e.g., Maximum Elevation, Maximum Depth,
 353 Volume, and Length-to-Depth Ratio), we retained only those 809 sinkholes with diameters \geq
 354 1 m.



356 **Figure 9.** Frequency distribution, represented as number of sinkholes and cumulative
 357 frequency in percentage, of different spatial and morphometric parameters of the inventoried
 358 sinkholes: (a) Azimuth; (b) Length; (c) Width; (d) Maximum elevation; (e) Maximum depth;
 359 (f) Perimeter; (g) Area; (h) Volume; (i) Elongation ratio; (j) Circularity index; (k)
 360 Compactness index; (l) Length to Depth ratio.



361
 362 **Figure 10.** Spatial distribution of the sinkholes categorized into different value ranges: (a)
 363 Length; (b) Maximum depth; (c) Perimeter; (d) Area; (e) Volume; (f) Elongation ratio; (g)
 364 Circularity index; (h) Compactness index; (i) Length to Depth ratio.

365 *4.3.1 Spatial parameters*

366 The analyzed spatial parameters include the orientation of the sinkholes (azimuth) and the
367 maximum elevation. The rose diagram in [Figure 9a](#) illustrates the frequency distribution of the
368 azimuth of the major axes of sinkholes, showing preferred N-S and W-E orientations. The
369 number of sinkholes in the Sunjiacha basin decreases as elevation increases ([Fig. 9d](#)). In the
370 relatively low elevation range of 1734~1860 m, there are 545 sinkholes (67.37%), whereas the
371 number of sinkholes at mid-elevations (1860~1960 m) and high elevations (1960~2071 m) are
372 216 (26.58%), and 48 (6.05%), respectively. Approximately 94% of the sinkholes are located
373 in the more dissected mid- and low- elevation areas, despite they represent 76% of the basin
374 area.

375 *4.3.2 Planimetric morphometric parameters*

376 The analyzed planimetric morphometric parameters include length, width, perimeter, area,
377 elongation ratio, circularity index, and compactness index. The frequency distribution of the
378 length ([Fig. 9b](#)) and width ([Fig. 9c](#)) of sinkholes follows a consistent pattern, characterized by
379 exponential decay as the values increase. The number of sinkholes with lengths and widths
380 ranging from 0 to 2 m is the highest, totaling 533 (44.64%) and 661 (55.36%), respectively.
381 Conversely, sinkholes exceeding 10 m in length and width account for only 7.45% and 4.19%
382 of the total sample, respectively. The map in [Figure 10a](#) reveals that sinkhole length exhibits
383 distinct spatial patterns, with smaller sinkholes preferentially occurring in areas with lower
384 degree of dissection (i.e., head of the basin and slopes close to the basin divides) and in recent
385 landslides associated with the trunk stream.

386 Regarding the ratio between length and width (elongation ratio, ER), [Basso et al. \(2013\)](#)
387 and [Zumpano et al. \(2019\)](#) classified the plan shape of sinkholes into five categories: circular
388 ($ER \leq 1.05$), sub-circular ($1.05 < ER \leq 1.21$), elliptical ($1.21 < ER \leq 1.65$), sub-elliptical
389 ($1.65 < ER \leq 1.8$), and elongated ($ER > 1.8$). [Figures 9i](#) and [10f](#) show that sinkholes tend to have
390 some degree of elongation, but without showing any clear spatial pattern in relation to this
391 parameter. Elliptical shapes dominate in the study area, with 618 sinkholes (51.76%), followed
392 by sub-circular morphologies with 384 depressions (32.16%). Elongated sinkholes also
393 represent a considerable number, totaling 93 (7.79%). Circular and sub-elliptical sinkholes are
394 relatively infrequent, with 35 (2.93%) and 64 (5.36%), respectively. Similar to length and width,
395 the frequency of sinkhole perimeter and area shows a general decreasing trend as the size
396 increases ([Figs. 9f, g](#)). The maximum perimeter and area reach 104 m and 662 m², respectively.
397 Sinkholes with a perimeter ≤ 4 m represent 21.9% (253) of the inventory, and 30.40% are those
398 with an area ≤ 1 m². In agreement with length and width, sinkholes with large perimeter and
399 area tend to occur in sectors of the basin where the drainage net shows a greater degree of
400 entrenchment, with the exception of some recent landslides ([Figs. 8b, 10c, and 10d](#)).

401 The circularity index (CLI) quantitatively assesses how much the shape of a sinkhole
402 deviates from a perfect circle. CLI is equal to 1 in the case of a perfect circular shape and attains
403 progressively lower values as it becomes less circular (e.g., elongated, irregular edge). The
404 circularity index statistics indicate that 89.87% (1,073 sinkholes), 60.64% (724 sinkholes), and
405 10.30% (123 sinkholes) of the mapped sinkholes have a CLI greater than 0.8, 0.9, and 0.96,
406 respectively ([Figs. 9j, 10g](#)). The compactness index (COI) also quantifies how close is the shape

407 of the sinkhole perimeter to a circle. The elongation and/or complexity of the sinkhole perimeter
408 contributes to reduce the *COI* below 1. The loess sinkholes with a *COI* greater than 0.6, 0.7,
409 and 0.8 represent 99.58% (1189 sinkholes), 96.40% (1151 sinkholes), and 27.72% (331
410 sinkholes) of the sinkholes, respectively (Figs. 9k, 10h). The statistics of both the *CLI* and *COI*
411 reveal that the perimeter of a great proportion of the sinkholes significantly deviates from a
412 circular shape, in agreement with the calculated elongation ratios. Moreover, these parameters
413 do not show any general spatial pattern, with the exception of a high proportion of sinkholes
414 with low *CLI* and *COI* values in some landslides associated with the trunk stream (Figs. 10g,
415 h).

416 **4.3.3 3D morphometric parameters**

417 The three-dimensional parameters are those that incorporate the vertical dimension,
418 including maximum depth, volume, and Length to Depth ratio. Note that large-area and large-
419 perimeter sinkholes may have reduced volume if their depth is low. The frequency distribution
420 of the maximum depth of the sinkholes in the study area shows a positively skewed distribution
421 (Fig. 9e). Sinkholes with depths ranging from 2 to 6 m represent 47.22% of the sample (382
422 sinkholes). Only 58 sinkholes exceed a maximum depth of 14 m, representing just 7.17% of the
423 total. The deepest sinkhole reaches a remarkable value of 29.6 m, and the average maximum
424 depth is 6.55 m. The frequency of the sinkhole volume decreases exponentially as the size
425 increases, with maximum and average values of 19,601 m³ and 335 m³, respectively (Fig. 9h).
426 A total of 428 sinkholes (52.90%) have volumes of ≤ 50 m³. The maps in Figures 10b and 10e
427 show that deeper sinkholes and large-volume sinkholes (>500 m³) preferentially occur in

428 association with deeply incised gullies.

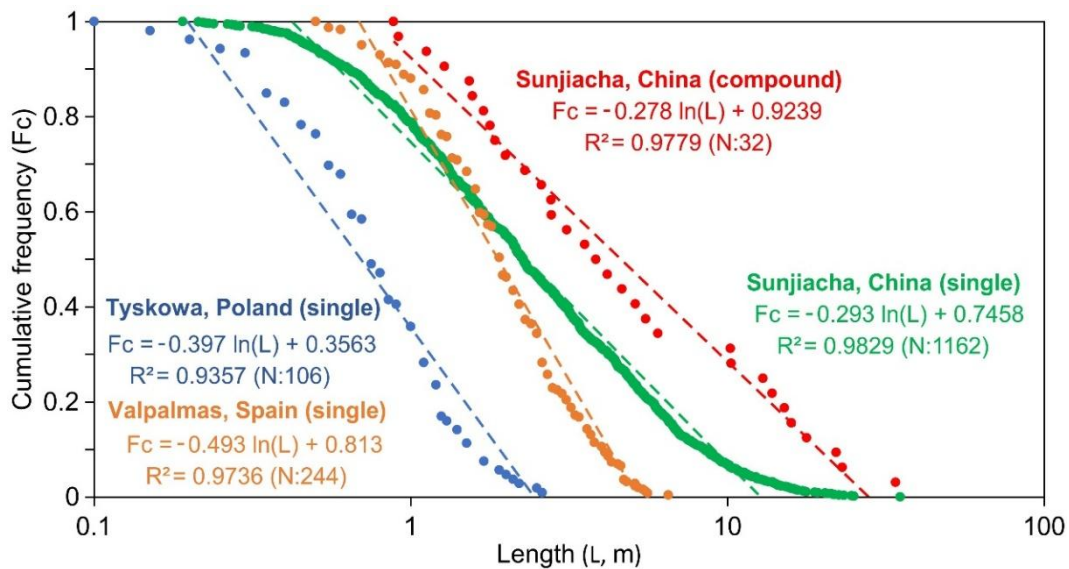
429 To some extent, the length and depth of the sinkholes reflect the horizontal and vertical
430 development of the depressions, respectively. Thus, the Length to Depth ratio (*LDr*) indicates
431 whether sinkholes have greater horizontal ($LDr > 1$) or vertical ($LDr < 1$) dimension. The
432 relative value of these parameters can be influenced by multiple factors and processes, some
433 favoring greater lengths (e.g., sinkhole expansion, coalescence) and others greater depth (e.g.,
434 deep subsurface conduits, erosion at the floor of sinkhole with bottom outlet). The frequency
435 distribution of the *LDr* shows a positively skewed distribution, with 569 sinkholes (70.33%)
436 having a *LDr* lower than 1 (greater depth than length), while those with a *LDr* greater than 1
437 represent 29.67% (240) of the sinkholes with depth data (Fig. 9I). These values indicate that
438 subsurface vertical erosion is the dominant process in the formation of loess sinkholes in the
439 study area, largely due to the development of relatively deep pipes within the thick loess cover
440 (Fig. 10i).

441 4.4 Frequency-size relationships

442 The semi-log plot in Figure 11 represents separately the length of the 1162 single sinkholes
443 and the 32 compound sinkholes mapped in the Sunjiacha basin, versus relative cumulative
444 frequency. The latter indicates the frequency of sinkholes equal or larger than a given length.
445 The length distribution of the single sinkholes, ranging from 35.1 m to 0.2 m and covering 2.3
446 orders of magnitude (i.e., $\log(\text{Max}/\text{Min})$), shows a wider range than the compound sinkholes,
447 spanning 1.6 orders of magnitude from 33.9 m to 0.9 m. As expected, compound sinkholes tend
448 to reach larger dimensions (i.e., plotted to the right), with a median length (cumulative

449 frequency = 0.5) that is 1.7 times larger than that of single sinkholes (3.8 m vs. 2.2 m).

450 In both cases, the empirical cumulative frequency-size distribution can be modelled
451 satisfactorily by logarithmic functions (natural logarithm) with a high goodness of fit ($R^2 > 0.97$).
452 The regression of the compound sinkholes describes adequately the distribution for the whole
453 length range. In contrast, the empirical distribution of the single sinkholes deviates from the
454 fitted curve for both small (< 0.4 m) and large dimensions (> 12.7 m). These cut-off or rollover
455 points indicate lower empirical frequencies for the smaller sinkholes and higher frequencies for
456 the larger ones compared to the regression curve. Given the completeness of the sinkhole
457 inventory, the lower rollover can be attributed to physical constraints, such as the minimum
458 span of a pipe-roof required for a collapse to occur. The upper rollover could be related to
459 factors such as the expansion of single sinkholes and the depth distribution of sinkhole-forming
460 underground pipes, which in the study area can reach significant depths given the considerable
461 thickness of the loess cover. Note that sinkholes reach a maximum depth of 29.6 m.

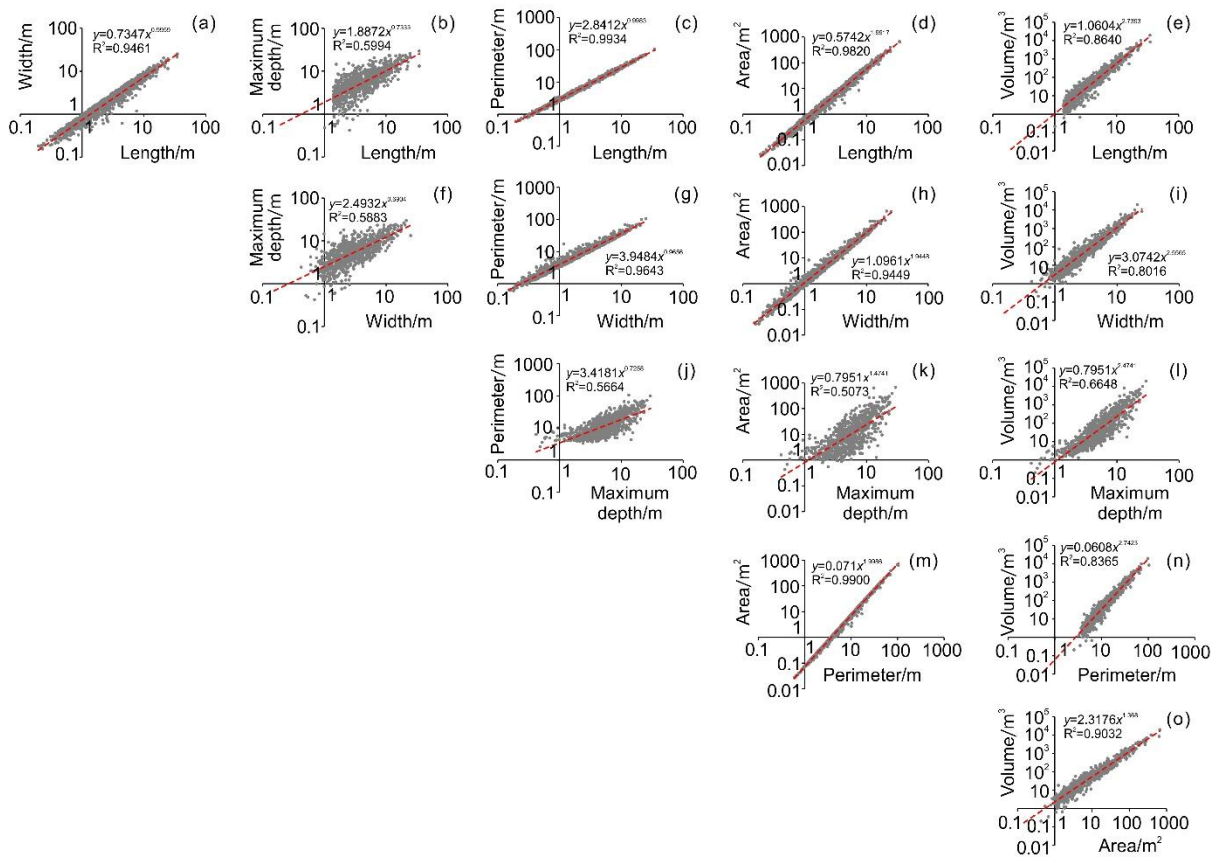


462
463 **Figure 11.** Graph showing the cumulative frequency-size distribution of single and compound
464 sinkholes in the study area, as well as single piping sinkholes in other regions with different

465 soils and environmental conditions (Tyskowa, Bieszczady Mountains, Poland; Valpalmas,
 466 Ebro Basin, NE Spain).

467 **4.5 Relationships between different parameters**

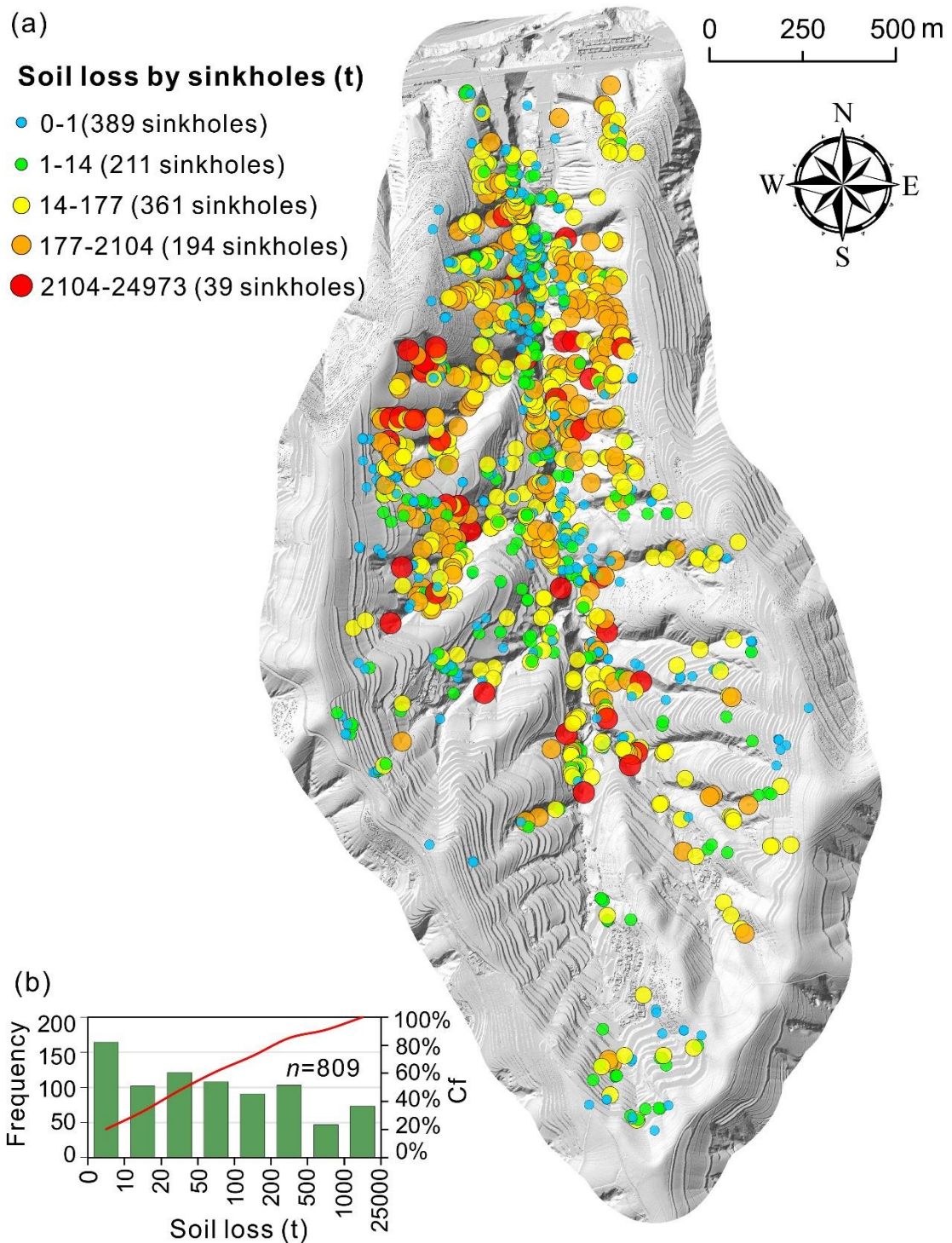
468 The planimetric (length, width, perimeter, area) and three-dimensional (maximum depth,
 469 volume) size parameters of the sinkholes were fitted pairwise in a matrix diagram showing
 470 graphically and with regressions (power functions) the relationships between each pair of
 471 morphometric parameters (Fig. 12). As expected, the regressions of pairs of planimetric
 472 parameters have always high goodness of fit $R^2 > 0.94$. In contrast, the relationship between
 473 planimetric and 3D parameters is poorer. R^2 is always below 0.6 for maximum depth, and less
 474 than 0.9 for volume.



475
 476 **Figure 12.** Matrix diagram illustrating the pairwise fitting relationships of planimetric (length,
 477 width, perimeter, area) and 3D (maximum depth, volume) morphometric parameters.

478 4.6 Subsurface soil erosion

479 Sinkhole development, including cavity-roof collapse and the expansion of sinkhole
480 margins by mass wasting processes, can contribute significantly to soil erosion, despite it is
481 largely overlooked worldwide. The complete and accurate sinkhole inventory constructed in
482 the Sunjiacha basin, including volumetric data, provides an excellent opportunity to assess the
483 impact of sinkhole-related soil erosion within the context of the Loess Plateau. We calculated
484 the soil loss associated with each sinkhole by multiplying the volume of each depression by the
485 soil's dry bulk density, as shown in **Figure 13a**. **Figure 13b** illustrates the frequency distribution
486 of soil loss related to individual sinkholes: 0~1 t (389 sinkholes, 32.58%); 1~14 t (211 sinkholes,
487 17.67%); 14~177 t (361 sinkholes, 30.23%); 177~2014 t (194 sinkholes, 16.25%); 2014~24973
488 t (39 sinkholes, 3.27%). The aggregate volume of sinkholes ($27.08 \times 10^4 \text{ m}^3$) multiplied by the
489 soil's dry bulk density (1.27 t/m^3) yields a total soil loss for the basin of $34.50 \times 10^4 \text{ t}$. Considering
490 the area of the basin (2400 ha), the specific soil erosion related to sinkholes can be estimated at
491 143.75 t/ha. Note that these values do not include hidden non-collapsed pipes. **Figure 13a** shows
492 that the impact of the process is quite uneven, with a much greater contribution in the lower
493 half of the basin and in the areas associated with deeply incised gullies.



494

495

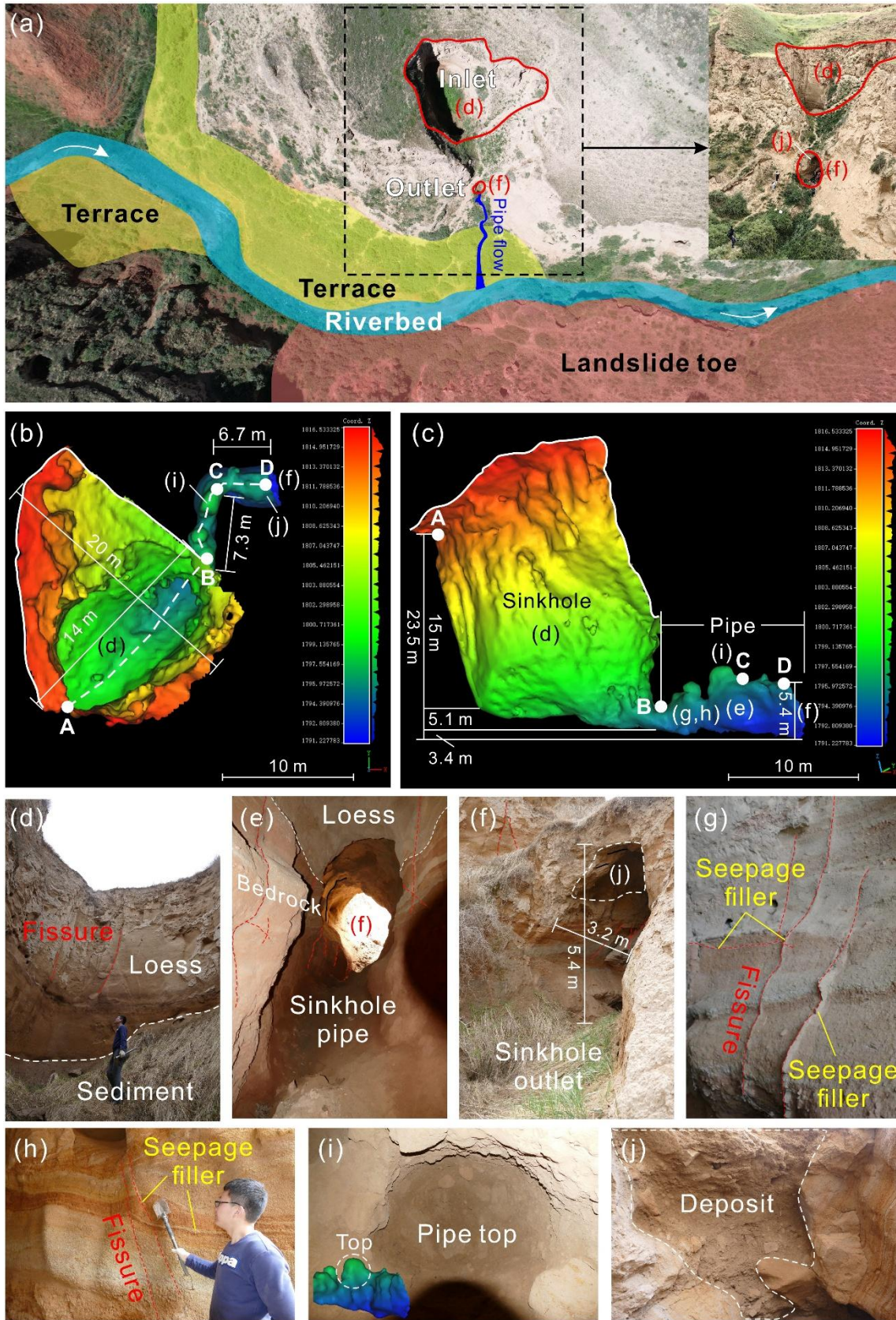
496

497

Figure 13. Soil loss by sinkholes: (a) Spatial distribution map indicating soil erosion related to individual sinkholes; (b) Histogram and cumulative frequency (Cf) curve of soil loss for individual sinkholes.

498 **4.7 In-depth investigation of a complex sinkhole**

499 Point clouds captured by airborne LiDAR surveys cover most of the sinkhole topography,
500 thanks to the vertical orientation of the sensors. However, obtaining comprehensive point
501 clouds of the interior of sinkholes remains challenging due to line-of-sight obstructions and the
502 complex morphology. To address the limitations of airborne LiDAR scanning, we employed a
503 handheld laser scanner to conduct a detailed investigation in the interior of thirteen
504 representative sinkholes. **Figures 14a-j** shows the field photographs and 3D models of a loess
505 sinkhole (HLS01). Morphometric measurements indicate that the perimeter of the sinkhole at
506 the land surface is 49.7 m, with an area of 179.6 m² and a maximum vertical depth of 20.1 m.
507 We adopted both the traditional method and the point cloud slicing algorithm to estimate the
508 volume of this sinkhole. The results show a volume and soil loss of 3610 m³ and 4585 t
509 calculated by the former method, while the latter yielded values of 1750 m³ and 2223 t,
510 respectively (**Table 3**). Because the fact that the sinkhole has an inclined top opening and a
511 sloping bottom underlain by deposits (**Figs. 14a, d**), the volume calculated by the traditional
512 method was twice higher than the actual volume. This finding also demonstrates that handheld
513 laser scanning can capture the complete geometry of the sinkhole more accurately, overcoming
514 the technical limitations of airborne LiDAR.



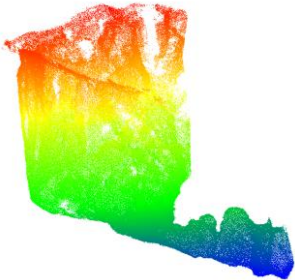
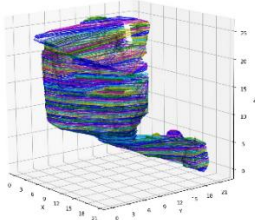
515

516

Figure 14. Detailed investigation of the interior of a representative sinkhole with an opening

517 at the bottom (see location in **Figs. 5a and f**): (a) Location, overview field photograph, and
 518 associated landforms; (b) 3D model generated from GeoSLAM point clouds, annotated with
 519 morphometric measurements; (c) Model slice along the AD profile line, also showing
 520 morphometric measurements; (d) Photograph of the sinkhole bottom; (e) Photograph of the
 521 pipe; (f) Sinkhole outlet; (g-h) Bedrock exposed in the sinkhole wall; (i) Photograph of the
 522 pipe top; (j) Poorly-sorted deposits including angular loess clasts accumulated in the sinkhole
 523 floor by collapse and mass wasting processes.

524 **Table 3** Comparison of sinkhole volume and corresponding soil loss estimated using
 525 traditional method versus point cloud slicing algorithm.

	Traditional method	Point cloud slicing algorithm
Data source	Airborne LiDAR	GeoSLAM LiDAR
Visualization		
	Vertical scanning by the UAS LiDAR	Multidirectional scanning by the handheld laser scanner.
Volume calculation principle	Volume= Area×Maximum depth (Gökkaya et al., 2021; De Waele and Gutiérrez, 2022)	 The convex hull algorithm is used to slice the point clouds at a thickness of 0.2 m. The volume of each slice is calculated and then summed up to obtain the total volume.
Soil loss (SL)	SL=ρ×V, where ρ is the dry density of soil, V is the volume of the sinkhole.	
Results	V: 3610 m ³ SL: 4585 t	V: 1750 m ³ (shaft 1606 m ³ , pipe 144 m ³) SL: 2223 t

526 Interestingly, most sinkholes examined in the field display dominant vertical development,
527 while this particular sinkhole exhibits a complex three-dimensional morphology comprising a
528 vertical shaft connected to a subhorizontal pipe. The upper shaft-like portion of the sinkhole
529 (20 m length \times 14 m width \times 20.1 m depth) is situated in loess deposits, while the lower portion
530 (14 m length \times 3.2 m width \times 5.4 m height) is a gently inclined ellipsoidal conduit carved into
531 horizontally bedded and jointed reddish sandstone. This lower conduit ends at the sinkhole
532 outlet perched 8 m above the valley floor (Fig. 14a). Unfortunately, due to the lack of precise
533 chronological evidence, we are unable to determine whether the initial development of this
534 sinkhole predates or postdates the valley incision. We interpret that the development of this
535 complex sinkhole started as a backward propagating conduit at the foot of the slope, associated
536 with a seepage outlet point controlled by joints in the loess cover and the bedrock (Figs. 14d-
537 h). Eventually, the enlarging conduit reached a sufficiently large span to initiate upward roof
538 collapse, ultimately originating the sinkhole. At present, five distinct ceiling cupolas can be
539 clearly observed at the top of this pipe (Figs. 14b, c and i), indicating sites of upward roof
540 propagation (stopping).

541 Additionally, we observed a significant accumulation of horizontally stratified flood
542 deposits resting atop the aeolian loess on the fluvial strath terrace (Fig. 14a). The interior of the
543 sinkhole is relatively cool and damp, with the bottom underlain by collapsed soil. We found
544 remnants of past flash-flood or debris-flow deposits on the sinkhole floor, as well as on the
545 walls and outlet ceiling of the connected lateral pipe (Figs. 14d, f, j). These sediments may
546 include: (1) Horizontally bedded deposits accumulated during floods in the drainage, with a

547 stage high enough to cause the penetration of flood waters into the sinkhole outlet
548 (backflooding); (2) Massive to poorly stratified deposits derived from collapse and mass
549 wasting processes acting primarily in the pipe roof and sinkholes margins, respectively. It
550 should be particularly noted that the largest loess landslide in this basin occurred on the opposite
551 bank of this sinkhole. Based on field investigations, we believe that this landslide completely
552 blocked the paleo-channel at that time, forming a small-scale dammed lake, and the landslide
553 deposits and lacustrine sediments could easily have entered the interior of the sinkhole through
554 lateral pipe.

555 **5 Discussion**

556 **5.1 Contributions of different factors to the sinkhole development**

557 The development of loess sinkholes is influenced by multiple factors of different nature,
558 such as topography, climate, hydrology, soil texture, joints and fissures, animal activity, plant
559 root systems, and human activity (Bernatek-Jakiel and Poesen, 2018; Peng et al., 2018; Geng
560 et al., 2021; Hu et al., 2022; Kariminejad et al., 2023; Li et al., 2024). At the scale of a small
561 basin, climate exhibits minimal variation. Therefore, we focus our analysis on the relationships
562 between loess sinkholes and variables related to catchment topography, geomorphology,
563 hydrology, and land use. In order to better understand the controlling factors, a number of
564 topographic and geomorphic indices and variables, such as Slope, Total Catchment Area (TCA),
565 Topographic Wetness Index (TWI), Valley Depth (VD), Channel Network Distance (CND),
566 Landslides, and Landuse, were computed with the open-source SAGA GIS platform and
567 subsequently mapped in ArcMap 10.5 (Figs. 15a-g). The selection of these indices and variables

568 is primarily based on the following considerations: (1) Slope governs the inherent hydraulic
569 gradient conditions for rainfall infiltration and surface runoff concentration, controlling the
570 piping process leading to sinkhole development; (2) Total Catchment Area represents the
571 upslope land surface that contributes surface and near-surface flow to a given outlet, pixel, or
572 stream segment (Gallant and Hutchinson, 2011). It is a proxy for the potential volume of water
573 that can reach a pipe or a sinkhole site, influencing on their initial formation and subsequent
574 morphological evolution; (3) Topographic Wetness Index is a steady-state, terrain-based proxy
575 for soil moisture and surface saturation potential. It quantifies the tendency of water to
576 accumulate at any location by integrating local slope with the upslope contributing area (Moore
577 et al., 1991); (4) Valley Depth is a measure of the vertical distance from a valley's highest ridges
578 down to its lowest points. It is a proxy for the degree of dissection; (5) Channel Network
579 Distance is the vertical height from a location to the nearest stream. Its value on valley margins
580 depends on both gradient and planimetric distance to the nearest drainage; (6) Landslides can
581 remodel the local topography and significantly disturb loess deposits, reducing their mechanical
582 strength and increasing their permeability, which in turn promotes piping and sinkhole
583 development; (7) Landuse mainly reflects the impact of human activity, notably terracing, on
584 piping and sinkhole development.

585 In order to assess the spatial relationships between sinkholes and the different indices and
586 variables, we calculated normalized frequencies for different intervals. This normalized
587 frequency (F_n) is given by the ratio between the proportion of sinkholes in the interval and the
588 proportion of the area of that interval. The higher the value of this 'likelihood ratio', the higher

589 the spatial concurrence between sinkholes and the areas with values within the interval (Figs.
590 15a1-g1). These data, together with the findings presented in the results, help to shed light on
591 the formation and spatial distribution of the loess sinkholes.

592 Overall, the normalized frequency graphs show that the distribution of sinkholes is
593 primarily controlled by hydrological, topographic and geomorphic factors. Water availability is
594 an essential factor, in as much as subsurface flow is the geomorphic agent responsible for piping
595 development. This is illustrated by the higher normalized frequencies of sinkholes in areas with
596 high Total Catchment Area ($>100 \text{ m}^2$; $F_n=2.97$) and high Topographic Wetness Index (>9 ;
597 $F_n=4.92$). Slope is the main governing topographic factor, which largely determines hydraulic
598 gradient and the erosional capability of subsurface flow. Sinkholes preferentially occur in high
599 gradient areas and close to incised gullies, with high Slope ($>40^\circ$; $F_n=1.82$), high Valley Depth
600 ($>10 \text{ m}$; $F_n=1.98$), low Channel Network Distance ($<1 \text{ m}$; $F_n=1.98$), and areas primarily
601 classified as erosional gullies ($F_n=2.53$). A good spatial correlation is also observed between
602 sinkholes and landslides, with a normalized frequency of sinkholes within landslides ($F_n=3.42$).
603 These spatial patterns are clearly recognizable in the detailed geomorphological map (Fig. 3)
604 and the Kernel density (Fig. 8a) and hot spot maps (Fig. 8b). The latter shows that sinkholes
605 developed on landslides tend to be smaller. This could be attributed to a younger age of those
606 sinkholes, developed on a more recent geomorphic surface.

607 The vast majority of the sinkholes occur in erosional gullies (71.44%, 853 sinkholes). This
608 pattern is consistent with findings reported for soil pipes in other regions worldwide (Verachtert
609 et al., 2010; Kariminejad et al., 2023). Incised gullies may foster the development of pipes and

610 sinkholes through various mechanisms (Bernatek-Jakiel and Poesen, 2018; Peng et al., 2018):
611 (1) they create steep hydraulic gradients; (2) they guide converging surface and subsurface
612 drainage; (3) they favor the development of inlet points (e.g., unloading cracks) and outlet
613 points for seepage flow. As shown in Figures 6c-f, rows of sinkholes occur along the bottom of
614 erosional gullies. These sinkholes can be connected through groundwater seepage channels, as
615 confirmed by electrical resistivity tomography surveys in previous studies (Hu et al., 2022). It
616 can be anticipated that, with the expansion and coalescence of the sinkholes, the gully will
617 experience significant entrenchment and will turn into a drainage dominated by surface flow.

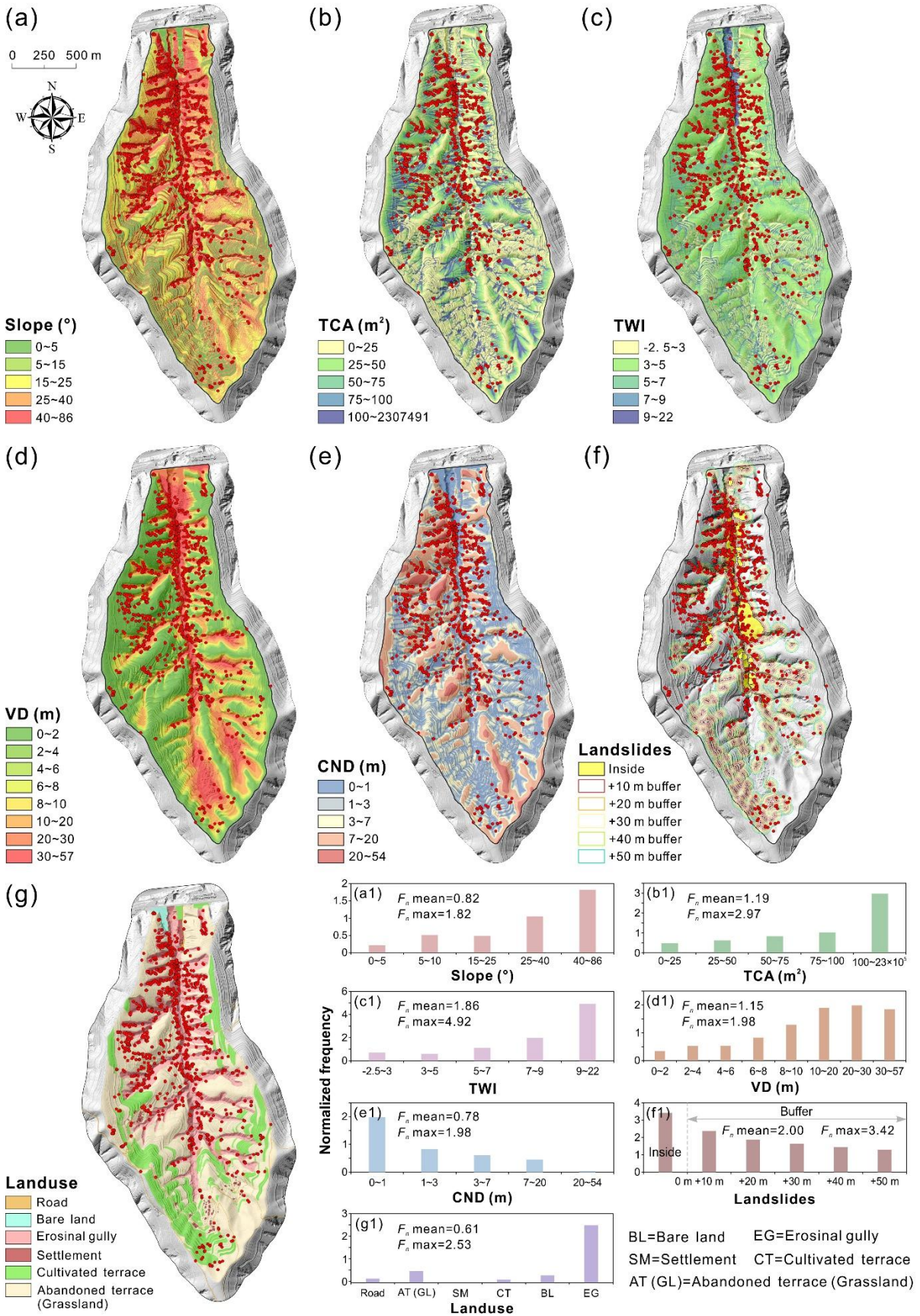
618 Another interesting feature is the close association between landslides and sinkholes in the
619 Sunjiacha basin. Previous studies have shown that soil pipes in slopes can favor efficient
620 drainage and, to some extent, help maintain slope stability (Pierson, 1983; Uchida et al., 2001;
621 Sidle and Bogaard, 2016). However, the sinkholes mapped on the landslides have mostly
622 formed after the development of the slope movements. The greater susceptibility of landslide
623 ground to piping and sinkhole development can be attributed to several factors: (1) landsliding
624 contributes to weaken the loess deposits; (2) the internal deformation of the landslide mass
625 typically involves a bulking effect (dilation and volume expansion) accompanied by an increase
626 in permeability; and (3) fissures and other pathways for focused water infiltration are common
627 on landslides (Hu et al., 2020, 2022). At some sites, a causal relationship between landslides
628 and sinkholes can be inferred, showing a cascading geomorphic effect. Figures 15f and fl
629 illustrate that landslides play an important role in the development of sinkholes. The distance
630 to landslides seems to control the development of sinkholes, but this control effect gradually

631 decays with increasing distance from the landslide boundary. Statistics show that as many as
632 251 sinkholes (accounting for 21%) have developed within the landslides, making the landslide
633 interior the second largest contributor to sinkhole formation ($F_n=3.42$). Approximately 43% of
634 sinkholes are distributed within the landslide and its outward 20m buffer zone ($F_n=1.87$). The
635 size of the sinkholes (e.g., length, area and volume), which can be considered as a proxy for
636 their age, seems to be influenced by the age of the geomorphic surface. Mature sinkholes tend
637 to be larger due to expansion and coalescence, and they usually occur on old geomorphic
638 surfaces (such as old gullies, river terraces and ancient landslides). Conversely, sinkholes
639 developed on landslides that have occurred in the past few years or decades tend to be smaller.
640 This pattern is clearly depicted in the hot spot map shown in **Figure 8b**.

641 We should be aware that the formation of soil pipes and sinkholes is not determined by a
642 single factor, but rather results from the interplay of interconnected geomorphic processes and
643 overlapping external influence factors (e.g., loess thickness, landscape position, surface and
644 subsurface flow, impermeable base layers, etc.). Conversely, the development of soil pipes and
645 sinkholes can further undermine slope stability, intensify gully erosion, and induce geological
646 hazards such as collapses, landslides, and debris flows.

647 In recent decades, due to a significant decrease in the local agricultural population and the
648 implementation of policies that promote the conversion of farmland back to forests and
649 grasslands, approximately 74% of the terraced fields have been taken out of cultivation. The
650 landuse map (**Figs. 15g, g1**) shows that abandoned terraces have reverted to grasslands in the
651 Sunjiacha basin. Abandoned terraces (25.63%, 306 sinkholes) appear to be more prone to

652 sinkhole formation than cultivated terraces (2.51%, 30 sinkholes). This can be related to more
653 favorable conditions for pipe development in the abandoned terraces and the lower preservation
654 potential of the sinkholes in the cultivated terraces, where sinkholes tend to be filled soon after
655 their formation. Without a doubt, pipe collapses and gully development pose threats to land
656 productivity, agricultural sustainability, soil nutrient levels, and the carbon cycle, while also
657 potentially destabilizing socio-economic conditions (Lena et al., 2024). By contrast, roads,
658 bare land, and settlement sites seem to exert almost no influence on sinkhole occurrence.



660 **Figure 15.** Spatial relationships between sinkholes and different indices and variables
661 expressed as maps (a-g) and normalized frequency graphs (a1-g1).

662 **5.2 Spatial and morphological features**

663 Sinkholes tend to be elongated and preferentially oriented in the Sunjiacha basin (Figs. 9a,
664 i). The majority of the major axes of the sinkholes align closely with the directions of the trunk
665 (N-S) and secondary (E-W) channels in the watershed (Fig. 3). These directions tend to guide:
666 (1) subsurface water flow and the trend of pipes generated by internal erosion, and (2) the
667 orientation of unloading cracks (e.g., scarped channel margins) through which water can
668 infiltrate. Both the pipes and the cracks influence the horizontal development of the sinkholes
669 by mass wasting processes acting on the margins and through coalescence (e.g., the merging of
670 aligned sinkholes connected to a common pipe).

671 The altitudinal distribution of sinkholes (Fig. 9d) may be governed by several factors: (1)
672 the density and entrenchment degree of the drainage network are higher at lower elevations; (2)
673 ground disturbed by landslides chiefly occurs in low elevation areas associated with the trunk
674 Sunjiacha stream; (3) high-elevation zones (e.g., rounded drainage divides) generally have
675 lower topographic gradient, lower degree of dissection, thinner loess cover, and more restricted
676 runoff contributing areas.

677 The deeper and larger sinkholes tend to be distributed in the more deeply incised valleys
678 (Figs. 10b, e). This pattern can be attributed to the development of deeper subsurface pipes in
679 areas with thicker loess, greater topographic gradient and lower local base level. Thicker loess
680 tends to accumulate in paleotopographic lows, which subsequently guide gully networks.

681 The goodness of fit between the planimetric and 3D parameters of the sinkholes is

682 relatively poor (Fig. 12). This indicates a limited dependence between the horizontal and
683 vertical dimensions of sinkholes, in agreement with the wide range shown by the Length to
684 Depth ratio (0~6). That is, sinkholes with small area can have significant depth and volume,
685 and sinkholes with limited volume can reach relatively large areas. This is also reflected by the
686 relatively poor fit shown between the two 3D parameters (volume and maximum depth;
687 $R^2=0.66$). Even so, the fitting equations presented in Figure 12 provide preliminary empirical
688 support for characterizing and predicting scaling relationships for sinkholes in the Loess Plateau.

689 **5.3 Frequency-size relationships of sinkholes in different soils and environments**

690 The cumulative frequency-size graph in Figure 11 shows that the length distribution of the
691 compound sinkholes (red) is clearly shifted towards larger dimensions with respect to the single
692 sinkholes (green). The average length of the compound and single sinkholes is 7.37 m and 3.65
693 m, respectively. This expected deviation in the size distribution can be explained by the different
694 sets of processes that operate in the development of the two sinkhole populations. The size of
695 the single sinkholes is related to pipe-roof collapse and the subsequent expansion of the scarped
696 edge of the depressions by erosional processes, mainly mass wasting and gullying. The size
697 tends to increase with the time elapsed since the initial collapse, as the sinkhole edge recedes.
698 Compound sinkholes result from the coalescence of adjoining and expanding sinkholes and/or
699 the occurrence of a new sinkhole intersecting a pre-existing one, leading to the sudden
700 enlargement of the depressions. The contribution of these processes (coalescence, intersection)
701 is influenced by the density and clustering degree of the sinkholes, in as much as the likelihood
702 of sinkhole aggregation is greater in tightly clustered sinkhole populations (Bernatek-Jakiel et

703 al., 2019; De Waele and Gutiérrez, 2022; Sevil and Gutiérrez, 2023). Moreover, sinkhole
704 merging entails a decrease in sinkhole density by number and a substantial increase in sinkhole
705 size.

706 **Figure 11** shows the cumulative frequency-length distribution of the single and compound
707 sinkholes mapped in the Sunjiacha basin, together with the single sinkholes inventoried in two
708 catchments with contrasting geological and climatic conditions (Bernatek-Jakiel et al., 2019):
709 Valpalmas in the Ebro Cenozoic Basin (NE Spain), and Tyskowa in the Bieszczady Mountains
710 of the Outer Eastern Carpathians (Poland). The pipe collapses in Valpalmas occur in Holocene
711 valley-fill alluvium consisting of indurated, Na-rich cohesive clayey silt that reaches around 8
712 m in thickness. Here, the climate is semiarid (mean precipitation 500 mm) and sinkholes tend
713 to occur associated with the edge of erosional scarps, showing a tightly clustered distribution.
714 The pipe collapses in the Tyskowa catchment can be considered as a representative sample of
715 those inventoried in several catchments of the Bieszczady Mts., characterized by a humid
716 climate (mean precipitation 900 mm; Bernatek-Jakiel et al., 2019). Here, sinkholes occur on
717 relatively thin slope deposits with some eolian component consisting of poorly indurated clayey
718 silt. The single sinkholes in Valpalmas (orange) show a similar size to the single sinkholes in
719 Sunjiacha for the central cumulative frequencies (i.e., F_c 0.5~0.6). Nonetheless, single
720 sinkholes in Valpalmas display a much narrower length range (1.1 vs. 2.3 orders of magnitude,
721 resulting in steeper curve) and significantly smaller maximum dimensions (6.5 m vs. 35.1 m).
722 The more restricted size range for the smaller sinkholes can be attributed to the fact that the
723 inventory in Valpalmas was restricted to sinkholes with lengths ≥ 0.5 m. The differences

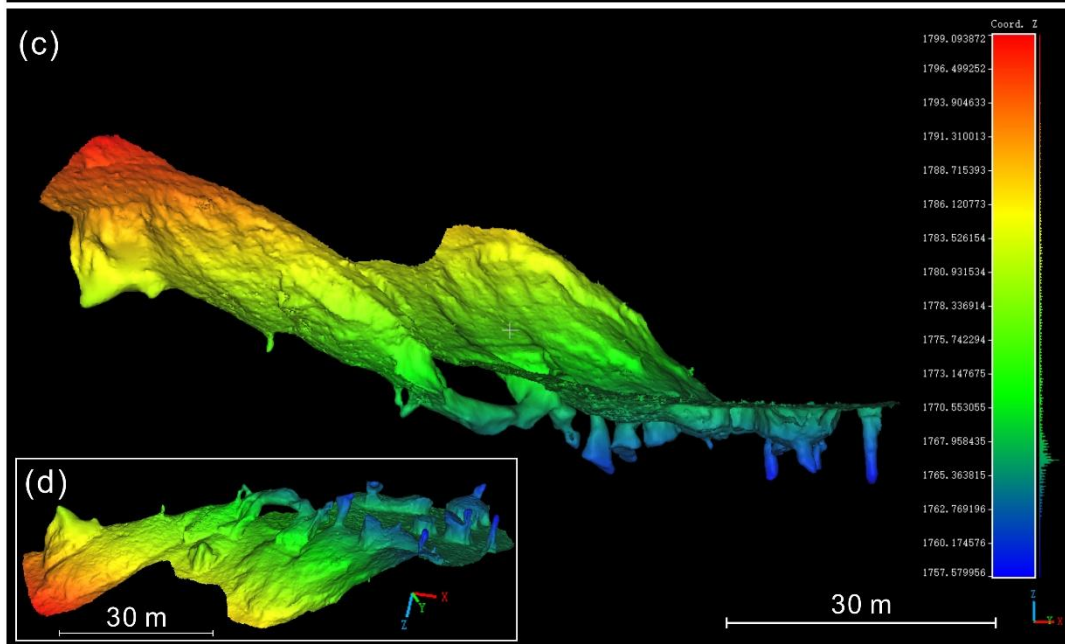
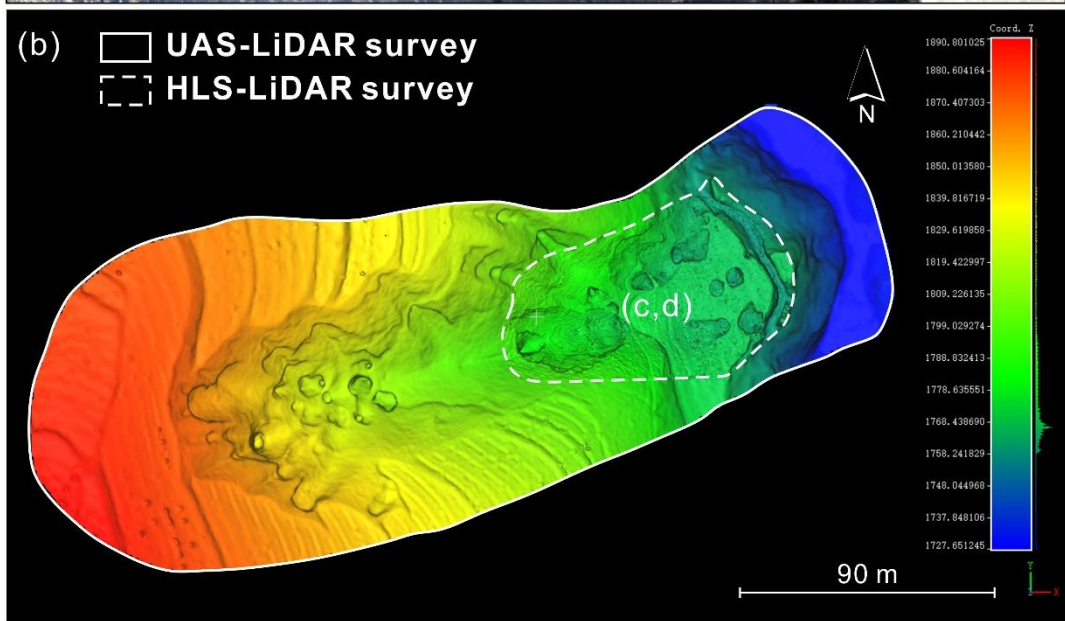
724 between Sunjiacha and Valpalmas can be ascribed to factors such as the greater morpho-
725 sedimentary diversity of Sunjiacha, where sinkholes occur in a broad range of deposits and
726 geomorphic settings (e.g., loess, colluvium, alluvium), and the wide depth range of sinkhole-
727 forming pipes, substantiated by the measured maximum depth of the sinkholes, ranging from
728 29.6 to 0.42 m (Figs. 9e, 10b and 14c). Single sinkholes in the humid Bieszczady Mts. of Poland
729 are much smaller, mainly because they occur on thinner and mechanically weaker deposits. The
730 weaker the soils, the smaller the largest span that can reach cavities before collapse. Induration
731 of the deposits by secondary carbonate (i.e., cementation) in this humid environment is less
732 significant than in the semiarid environments of Valpalmas and the Loess Plateau.

733 **5.4 Limitations and prospects**

734 Extensive field surveys reveal that loess sinkholes possess highly complex three-
735 dimensional morphologies, rather than being simple cylindrical or conical features (Figs. 6i, 7c,
736 14b and 16; Hu et al., 2024). This is illustrated by the high-resolution scanning of 142 sinkholes
737 with a handheld laser device carried out in 2021 in a small basin, named Laozigou, east of our
738 study area (Hu et al., 2024; Jiang et al., 2024). The data can be accessed at
739 <https://doi.org/10.1016/j.geomorph.2024.109404>. As shown in Table 3, volume estimates based
740 on airborne LiDAR point clouds and simplified volume estimation methods can lead to highly
741 inaccurate approximations. The aggregate volume, and hence the inferred soil loss reported in
742 our study area may therefore be overestimated. Several factors may contribute to the deviation
743 between the actual volume and the volume calculated, leading to over- or under-estimations: (1)
744 volumes are calculated using maximum depth and assuming a cylindrical geometry, but

745 sinkholes may be conical (overestimation) or the actual depth may be deeper (underestimation);
746 (2) sinkholes may be connected to conduits that cannot be imaged in airborne surveys, resulting
747 in underestimations.

748 Encouragingly, the comprehensive point clouds acquired by the handheld scanner enable
749 us to develop far more precise cloud-slicing and volumetric-integration algorithms for exact
750 volume computation (Hu et al., 2024). This will enable us to develop a more reliable fitting
751 formula relating sinkhole area and volume, which could be used for refining the results obtained
752 from the UAS surveys. We conducted a survey of a gully by jointly employing UAS-LiDAR
753 and HLS-LiDAR technologies and found that the integrated point cloud data can effectively
754 delineate the internal structure and connectivity of sinkholes, as they overcome the limitations
755 of a single LiDAR technology. Meanwhile, machine-learning approaches for the automatic
756 detection and delineation of sinkholes are rapidly emerging and showing promising results (Zhu
757 et al., 2016, 2020; Jiang et al., 2024; Li et al., 2024; Coşkuner et al., 2025; Creati et al., 2025).
758 Indeed, we have already implemented an end-to-end workflow that couples airborne LiDAR
759 point clouds with deep-learning models to achieve automatic sinkhole identification, instance
760 segmentation, feature extraction, cataloguing, and mapping (Li et al., 2025).



762 **Figure 16.** Integrated sinkhole investigation combining UAS-LiDAR and HLS-LiDAR: (a)
763 Coverage areas of the two LiDAR surveys; (b) The mesh model generated from the fused
764 point cloud data; (c) The side view of mesh model from the HLS-LiDAR survey area; (d) The
765 bottom view of **c**.

766 **6 Data availability**

767 The dataset supporting this study is openly available on Zenodo at
768 <https://doi.org/10.5281/zenodo.14000267> (Hu et al., 2025).

769 **7 Conclusions**

770 High-resolution models derived from photographs and LiDAR data captured with a UAS
771 have allowed the production of a comprehensive cartographic inventory of loess sinkholes in a
772 catchment (2.4 km²) of the Chinese Loess Plateau with a high density of sinkholes (ca. 500
773 sinkholes/km²). The spatial data, including a bare-surface digital elevation model and a 3D
774 terrain point cloud, proved suitable for accurately mapping the sinkholes, differentiating
775 between single (1194) and compound depressions (288), and extracting precise planimetric
776 morphometric parameters. This is the first morphometric dataset available for the piping-related
777 sinkholes of the CLP. Three dimensional parameters such as depth and volume can be also
778 extracted or estimated, although with much higher uncertainty. Rough cumulative volume
779 estimates yield sinkhole-related soil erosion values of around 140 t/ha. The work illustrates that
780 the limitations of the airborne data for measuring 3D morphometric parameters can be
781 overcome by using SLAM-based handheld scanners. The 3D point clouds obtained with these
782 devices at specific sinkholes, although labor intensive, allow precise measurement of the
783 volume of the scanned voids. Nonetheless, hidden pipes, which may account for a significant

784 volume of subsurface erosion, remain elusive for these direct surveying techniques.

785 The sinkholes in the analyzed catchment tend to be elongated (52% with elongation ratio
786 between 1.21 and 1.65) and preferentially oriented following the dominant trends of the
787 drainage network. They show a broad range of dimensions, ranging from 0.19 to 35.11 m in
788 length (2.3 orders of magnitude). As expected, compound sinkholes tend to be significantly
789 larger than single sinkholes (7.37 m vs. 3.65 m in average length, respectively), although the
790 degree of coalescence is rather moderate (single 97.3%; compound 2.7%). A remarkable feature
791 of the investigated sinkholes is their large vertical dimension. Around 70% of the sinkholes
792 have a greater depth than length. The average and maximum depths are 6.5 m and 29.6 m,
793 respectively, indicating the development of deep-seated pipes in thick loess cover or even within
794 the jointed and friable sandstone bedrock. Comparison with other morphometric datasets from
795 semiarid Spain (fine grained alluvium) and humid Poland (thin loess-rich colluvium) reinforces
796 the large size of the studied sinkholes in the Chinese loess, developed on much thicker loess
797 and generally rooted in deeper pipes.

798 The spatial relationships between the sinkholes and other geomorphic features and various
799 topographic and hydrologic indices reveal that their development is mainly controlled by the
800 amount of water available for subsurface flow (i.e., runoff contributing area) and topographic
801 gradient. Sinkholes occur preferentially along the steep margins of deeply incised streams and
802 gully networks. Recent landslides, underlain by weakened and more porous disturbed loess
803 deposits are also identified as areas especially prone to piping and sinkhole occurrence.

804 **Author contributions.**

805 SH, FG, FZ, and SL designed the study and wrote the manuscript. SH, FG, and SL
806 compiled and analyzed the dataset. SH, XW, JS, and SW performed field investigation. NW,
807 XL, and FG supervised and reviewed the manuscript. All authors contributed to the writing and
808 editing of this paper.

809 **Competing interests.**

810 The contact author has declared that neither they nor their co-authors have any competing
811 interests.

812 **Disclaimer.**

813 Publisher's note: Copernicus Publications remains neutral with regard to jurisdictional
814 claims in published maps and institutional affiliations

815 **Acknowledgements.**

816 The authors are grateful to Dr. Anita Bernatek-Jakiel for providing published
817 morphometric data on piping sinkholes in the Valpalmas (Spain) and the Tyskowa (Poland)
818 catchments. The work by FG has been supported by the project DIAPERNO (PID2021-
819 123189NB-I00) of the Spanish Government (Ministerio de Ciencia e Innovación). FG belongs
820 to the IUCA and the Geoenvironmental Processes and Global Change (E02_23R) research
821 group financed by the Aragón Government and the European Social Fund (ESF-FSE). We
822 would also like to thank Dr. Yixian Chen for his participation in the fieldwork.

823 **Financial support.**

824 This research has been supported by the National Natural Science Foundation of China

825 (grant nos. 42371009, 42001006 and 42230712), the National Key Research and Development
826 Program of China (grant nos. 2022YFC3003401 and 2023YFC3008401).

827 **Review statement.**

828 This paper was edited by Giulio G.R. Iovine and reviewed by Christian Sommer and one
829 anonymous referee.

830 **References**

- 831 Basso, A., Bruno, E., Parise, M., and Pepe, M.: Morphometric analysis of sinkholes in a karst
832 coastal area of southern Apulia (Italy), *Environ. Earth Sci*, 70, 2545–2559, 2013.
- 833 Bernatek, A.: The Influence of Piping on Mid-Mountain Relief: A Case Study from the Polish
834 Bieszczady Mts. (Eastern Carpathians), *Carpath J Earth Env*, 10, 107–120, 2015.
- 835 Bernatek-Jakiel, A., Jakiel, M., and Krzemień, K.: Piping dynamics in mid-altitude mountains
836 under a temperate climate: Bieszczady Mountains, eastern Carpathians, *Earth Surf Proc*
837 *Land*, 42, 1419–1433, 10.1002/esp.4160, 2017.
- 838 Bernatek-Jakiel, A. and Kondracka, M.: Combining geomorphological mapping and near
839 surface geophysics (GPR and ERT) to study piping systems, *Geomorphology*, 274, 193–
840 209, 2016.
- 841 Bernatek-Jakiel, A. and Poesen, J.: Subsurface erosion by soil piping: significance and research
842 needs, *Earth-Sci Rev*, 185, 1107–1128, 10.1016/j.earscirev.2018.08.006, 2018.
- 843 Bernatek-Jakiel, A., Gutiérrez, F., Nadal-Romero, E., and Jakiel, M.: Exploring the frequency-
844 size relationships of pipe collapses in different morphoclimatic regions, *Geomorphology*,
845 345, 106845, 10.1016/j.geomorph.2019.106845, 2019.
- 846 Borah, U. K., Gond, A., Rajan, P. P., Sivan, R., and Vivekanandan, N.: Joint geomorphological
847 and geophysical (electrical resistivity) investigation for the configuration of soil pipe,
848 *Contrib Geophys Geod*, 52, 239–255, 10.31577/congeo.2022.52.2.4, 2022.
- 849 Bruno, E., Calcaterra, D., and Parise, M.: Development and morphometry of sinkholes in
850 coastal plains of Apulia, southern Italy. Preliminary sinkhole susceptibility assessment,

851 Eng Geol, 99, 198–209, 10.1016/j.enggeo.2007.11.017, 2008.

852 Cole, J. P.: Study of major and minor civil divisions in political geography, The 20th
853 international geographical congress, London, 1964.

854 Coskuner, B., Ince, İ., and Barstuğan, M.: Sinkhole detection via deep learning using DEM
855 images, Nat Hazards, 121, 8347–8366, 10.1007/s11069-025-07127-0, 2025.

856 Creati, N., Paganini, P., Sterzai, P., and Pavan, A.: Mapping of karst sinkholes from LIDAR
857 data using machine-learning methods in the Trieste area, J Spat Sci, 70, 365–380,
858 10.1080/14498596.2025.2469176, 2025.

859 Day, M.: Doline morphology and development in Barbados, Annals of the Association of
860 American Geographers, 73, 206–219, 1983.

861 De Carvalho Júnior, O. A., Guimarães, R. F., Montgomery, D. R., Gillespie, A. R., Gomes, R.
862 A. T., De Souza Martins, É. D., and Silva, N. C.: Karst Depression Detection Using
863 ASTER, ALOS/PRISM and SRTM-Derived Digital Elevation Models in the Bambu
864 Group, Brazil, Remote Sens, 6, 330–351, 10.3390/rs6010330, 2014.

865 De Waele, J. and Gutiérrez, F.: Karst hydrogeology, geomorphology and caves, John Wiley &
866 Sons, 888 p, 2022.

867 Donnelly, L. J.: Subsidence and associated ground movements on the Pennines, northern
868 England, Q J Eng Geol Hydroge, 41, 315–332, Doi 10.1144/1470-9236/07-216, 2008.

869 Farrant, A. R. and Cooper, A. H.: Karst geohazards in the UK: the use of digital data for hazard
870 management, Q J Eng Geol Hydroge, 41, 339–356, Doi 10.1144/1470-9236/07-201, 2008.

871 Gallant, J. C. and Hutchinson, M. F.: A differential equation for specific catchment area, Water
872 Resour Res, 47, W05535, 10.1029/2009wr008540, 2011.

873 Gao, Y., Alexander, E. J. R., and Barnes, R. J.: Karst database implementation in Minnesota:
874 analysis of sinkhole distribution, Environ Geol, 47, 1083–1098, 10.1007/s00254-005-
875 1241-2, 2005.

876 Gao, Y., Alexander, E.C., Tipping, R.: The development of a karst feature database for
877 southeastern Minnesota. J. Cave Karst Stud. 64, 51–57, 2002.

878 Geng, H. P., Liu, R., Zheng, W. S., Zhang, Y. B., Xie, R., Guo, Y., and Pan, B. T.: Interaction

879 Between Animal Burrowing and Loess Cave Formation in the Chinese Loess Plateau,
880 *Front Earth Sci*, 9, 806921, 10.3389/feart.2021.806921, 2021.

881 Geng, H. P., Xu, W. Y., Zheng, W. S., Gao, X. L., and Pan, B. T.: A hybrid mechanism for the
882 initiation and expansion of loess caves across the Chinese Loess Plateau, *Land Degrad*
883 *Dev*, 34, 3329–3339, 10.1002/ldr.4686, 2023.

884 Gibbs, H.S.: Tunnel-gully erosion on the Wither Hills, Marlborough. *New Zealand Journal of*
885 *Science and Technology* 27(A2), 135–146, 1945.

886 Gökkaya, E., Gutiérrez, F., Ferk, M., and Görüm, T.: Sinkhole development in the Sivas gypsum
887 karst, Turkey, *Geomorphology*, 386, 107746, 10.1016/j.geomorph.2021.107746, 2021.

888 Gutiérrez, F., Desir, G., and Gutiérrez, M.: Causes of the catastrophic failure of an earth dam
889 built on gypsiferous alluvium and dispersive clays (Altorricón, Huesca Province, NE
890 Spain), *Environ Geol*, 43, 842–851, 10.1007/s00254-002-0700-2, 2003.

891 Gutiérrez, F., Parise, M., De Waele, J., and Jourde, H.: A review on natural and human-induced
892 geohazards and impacts in karst, *Earth-Sci Rev*, 138, 61–88,
893 10.1016/j.earscirev.2014.08.002, 2014.

894 Hofierka, J., Gally, M., Bandura, P., and Šašák, J.: Identification of karst sinkholes in a forested
895 karst landscape using airborne laser scanning data and water flow analysis,
896 *Geomorphology*, 308, 265–277, 10.1016/j.geomorph.2018.02.004, 2018.

897 Hu, S., Gutiérrez, F., Zhang, F., Li, S., Wang, N., Li, X., and Wang, X.: A morphological dataset
898 of loess sinkholes from a small basin in the Chinese Loess Plateau (1.0) [Data set]. Zenodo.
899 <https://doi.org/10.5281/zenodo.14000267>, 2025.

900 Hu, S., Jiang, Z.D., Wang, N.L., Zhang, F.Y., Chen, Y.X., Wu, S.B., Wang, L., Li, S.S.: In Situ
901 Dataset of Loess Sinkholes using UAS and LiDAR Technology in Huining County, China
902 (2024). *Digital Journal of Global Change Data Repository*,
903 <https://doi.org/10.3974/geodb.2024.05.05.V1>, 2024.

904 Hu, S., Qiu, H. J., Wang, N. L., Cui, Y. F., Wang, J. D., Wang, X. G., Ma, S. Y., Yang, D. D.,
905 and Cao, M. M.: The influence of loess cave development upon landslides and
906 geomorphologic evolution: A case study from the northwest Loess Plateau, China,

907 Geomorphology, 359, 107167, 10.1016/j.geomorph.2020.107167, 2020.

908 Hu, S., Qiu, H. J., Wang, N. L., Wang, X. G., Ma, S. Y., Yang, D. D., Wei, N., Liu, Z. J., Shen,
909 Y. D., Cao, M. M., and Song, Z. P.: Movement process, geomorphological changes, and
910 influencing factors of a reactivated loess landslide on the right bank of the middle of the
911 Yellow River, China, *Landslides*, 19, 1265–1295, 10.1007/s10346-022-01856-0, 2022.

912 Jiang, Z. D., Hu, S., Deng, H., Wang, N. L., Zhang, F. Y., Wang, L., Wu, S. B., Wang, X. A.,
913 Cao, Z. W., Chen, Y. X., and Li, S. S.: Detection and automatic identification of loess
914 sinkholes from the perspective of LiDAR point clouds and deep learning algorithm,
915 *Geomorphology*, 465, 109404, 10.1016/j.geomorph.2024.109404, 2024.

916 Jones, E. and Beck, D.: The use of three-dimensional laser scanning for deformation monitoring
917 in underground mines, *Proceedings of the 13th AusIMM Underground Operators*
918 *Conference*: 66, 267–270, 2017.

919 Kariminejad, N., Sepehr, A., Poesen, J., and Hassanli, A.: Combining UAV remote sensing and
920 pedological analyses to better understand soil piping erosion, *Geoderma*, 429, 116267,
921 10.1016/j.geoderma.2022.116267, 2023.

922 Kim, C. E. and Anderson, T. A.: Digital disks and a digital compactness measure, *Proceedings*
923 *of the sixteenth annual ACM symposium on Theory of computing*, ACM Press, New York,
924 117–124, 1984.

925 Kobal, M., Bertonecjl, I., Pirotti, F., Dakskobler, I., and Kutnar, L.: Using Lidar Data to Analyse
926 Sinkhole Characteristics Relevant for Understory Vegetation under Forest Cover-Case
927 Study of a High Karst Area in the Dinaric Mountains, *Plos One*, 10, e0122070,
928 10.1371/journal.pone.0122070, 2015.

929 Konsolaki, A., Vassilakis, E., Gouliotis, L., Kontostavlos, G., and Giannopoulos, V.: High
930 Resolution Digital 3d Modelling of Subsurface Morphological Structures of Koutouki
931 Cave, Greece, *Acta Carsologica*, 49, 163–177, 10.3986/ac.v49i2-3.7708, 2020.

932 Lee, E. J., Shin, S. Y., Ko, B. C., and Chang, C.: Early sinkhole detection using a drone-based
933 thermal camera and image processing, *Infrared Phys Techn*, 78, 223–232,
934 10.1016/j.infrared.2016.08.009, 2016.

935 Li, S., Sun, J., Hu, S., & Wang, L. (2025). LSPNet for Automatic Recognition and Cataloguing
936 of Loess Sinkholes from Point Clouds (V1.0). Zenodo.
937 <https://doi.org/10.5281/zenodo.17667244>

938 Li, S. S., Hu, S., Wang, L., Zhang, F. Y., Wang, N. L., Wu, S. B., Wang, X. A., and Jiang, Z. D.:
939 Quantifying the Geomorphological Susceptibility of the Piping Erosion in Loess Using
940 LiDAR-Derived DEM and Machine Learning Methods, *Remote Sens*, 16, 4203,
941 10.3390/rs16224203, 2024.

942 Li, W. W., Goodchild, M. F., and Church, R.: An efficient measure of compactness for two-
943 dimensional shapes and its application in regionalization problems, *Int J Geogr Inf Sci*, 27,
944 1227–1250, 10.1080/13658816.2012.752093, 2013.

945 Li, X., Song, Y., and Ye, W.: Engineering geological research on tunnel-erosion in loess, Tongji
946 University Press, Shanghai, 2010. (in Chinese)

947 Li, X. A., Wang, L., Hong, B., Li, L. C., Liu, J., and Lei, H. N.: Erosion characteristics of loess
948 tunnels on the Loess Plateau: A field investigation and experimental study, *Earth Surf Proc*
949 *Land*, 45, 1945–1958, 10.1002/esp.4857, 2020.

950 Llana, M., Carreras, S., Bernatek-Jakiel, A., Ollero, A., and Nadal-Romero, E.: Agricultural
951 land abandonment linked to pipe collapse and gully development: Reconstruction from
952 archival SfM and LiDAR datasets, *Geoderma*, 449, 116995,
953 <https://doi.org/10.1016/j.geoderma.2024.116995>, 2024.

954 Liu, H. X. and Wang, L.: Mapping detention basins and deriving their spatial attributes from
955 airborne LiDAR data for hydrological applications, *Hydrol Process*, 22, 2358–2369,
956 10.1002/hyp.6834, 2008.

957 Liu, T.S.: Loess Deposits in the Middle Reaches of the Yellow River, Science Press, Beijing,
958 1–234, 1964. (in Chinese)

959 Liu, T.S.: Loess Deposits in China, Science Press, Beijing, 1–244, 1965. (in Chinese)

960 Panno, S. V. and Luman, D. E.: Mapping palimpsest karst features on the Illinois sinkhole plain
961 using historical aerial photography, *Carbonate Evaporite*, 28, 201–214, 10.1007/s13146-
962 012-0107-4, 2013.

963 Mokroš, M., Mikita, T., Singh, A., Tomašík, J., Chudá, J., Wężyk, P., Kuželka, K., Surový, P.,
964 Klimánek, M., Zieba-Kulawik, K., Bobrowski, R., and Liang, X. L.: Novel low-cost
965 mobile mapping systems for forest inventories as terrestrial laser scanning alternatives, *Int*
966 *J Appl Earth Obs*, 104, 102512, 10.1016/j.jag.2021.102512, 2021.

967 Moore, I. D., Grayson, R., and Ladson, A.: Digital terrain modelling: a review of hydrological,
968 geomorphological, and biological applications, *Hydrol Process*, 5, 3–30, 1991.

969 Morgan, R. P. C.: Soil erosion and conservation, 3rd edition, Blackwell Publishing, the United
970 Kingdom, 2005.

971 Niu, Y. N.: Study on provenance of Quaternary loess in Longxi area: a case from Huining,
972 Lanzhou University Thesis, 2023. (in Chinese)

973 Öztürk, M. Z., Şener, M. F., Şener, M., and Şimşek, M.: Structural controls on distribution of
974 dolines on Mount Anamas (Taurus Mountains, Turkey), *Geomorphology*, 317, 107–116,
975 10.1016/j.geomorph.2018.05.023, 2018.

976 Panno, S., Weibel, C. P., and Li, W.: Karst regions of Illinois, Open file series 1997-02,
977 <http://hdl.handle.net/10111/UIUCOCA:karstregionsofil19972pann>, 1997.

978 Peng, J. B., Sun, P., Igwe, O., and Li, X.: Loess caves, a special kind of geo-hazard on loess
979 plateau, northwestern China, *Eng Geol*, 236, 79–88, 10.1016/j.enggeo.2017.08.012, 2018.

980 Peng, S.S.: Pronounced changes in atmospheric circulation and dust source areas during the
981 mid-Pleistocene implicated by the Huining loess-soil sequence from the northeastern
982 margin of the Tibetan Plateau, China University of Geosciences (Beijing) PhD Thesis,
983 2014. (in Chinese)

984 Pierson, T. C.: Soil pipes and slope stability, *Q. J. Eng. Geol. Hydrogeol.*, 16, 1-11, 1983.

985 Poesen, J.: Soil erosion in the Anthropocene: Research needs, *Earth Surf Proc Land*, 43, 64–84,
986 10.1002/esp.4250, 2018.

987 Rajabi, A.: Sinkhole Detection and Quantification Using LiDAR Data. Electronic Theses and
988 Dissertations, 5776. <https://stars.library.ucf.edu/etd/5776>, 2018.

989 Richards, K. S. and Reddy, K. R.: Critical appraisal of piping phenomena in earth dams, *B Eng*
990 *Geol Environ*, 66, 381–402, 10.1007/s10064-007-0095-0, 2007.

- 991 Sevil, J. and Gutiérrez, F.: Morphometry and evolution of sinkholes on the western shore of the
992 Dead Sea. Implications for susceptibility assessment, *Geomorphology*, 434, 108732,
993 10.1016/j.geomorph.2023.108732, 2023.
- 994 Sidle, R. C. and Bogaard, T. A.: Dynamic earth system and ecological controls of rainfall-
995 initiated landslides, *Earth-Sci Rev*, 159, 275–291, 10.1016/j.earscirev.2016.05.013, 2016.
- 996 Uchida, T., Kosugi, K., and Mizuyama, T.: Effects of pipeflow on hydrological process and its
997 relation to landslide: a review of pipeflow studies in forested headwater catchments,
998 *Hydrol Process*, 15, 2151–2174, DOI 10.1002/hyp.281, 2001.
- 999 Vajedian, S. and Motagh, M.: Extracting sinkhole features from time-series of TerraSAR-
1000 X/TanDEM-X data, *ISPRS-J Photogramm Remote Sens*, 150, 274–284,
1001 10.1016/j.isprsjprs.2019.02.016, 2019.
- 1002 Vennari, C. and Parise, M.: A Chronological Database about Natural and Anthropogenic
1003 Sinkholes in Italy, *Geosciences*, 12, 200, 10.3390/geosciences12050200, 2022.
- 1004 Verachtert, E., Van den Eeckhaut, M., Poesen, J., and Deckers, J.: Factors controlling the spatial
1005 distribution of soil piping erosion on loess-derived soils: A case study from central
1006 Belgium, *Geomorphology*, 118, 339–348, 10.1016/j.geomorph.2010.02.001, 2010.
- 1007 Wang, X. G., Hu, S., Lian, B. Q., Wang, J. D., Zhan, H. B., Wang, D. Z., Liu, K., Luo, L., and
1008 Gu, C. Y.: Formation mechanism of a disaster chain in Loess Plateau: A case study of the
1009 Pucheng County disaster chain on August 10, 2023, in Shaanxi Province, China, *Eng Geol*,
1010 331, 107463, 10.1016/j.enggeo.2024.107463, 2024.
- 1011 Wu, Q. S., Deng, C. B., and Chen, Z. Q.: Automated delineation of karst sinkholes from LiDAR-
1012 derived digital elevation models, *Geomorphology*, 266, 1–10,
1013 10.1016/j.geomorph.2016.05.006, 2016.
- 1014 Yang, S. and Ding, Z.: Spatial changes in grain size of loess deposits in the Chinese Loess
1015 Plateau and implications for palaeoenvironment, *Quaternary Sciences*, 37, 934–944, 2017.
1016 (in Chinese)
- 1017 Yuan, Z. L., Ban, X. J., Han, F. Y., Zhang, X. Q., Yin, S. H., and Wang, Y. M.: Integrated three-
1018 dimensional visualization and soft-sensing system for underground paste backfilling, *Tunn*

1019 Undergr Sp Tech, 127, 104578, 10.1016/j.tust.2022.104578, 2022.

1020 Zhang, F., Peng, J., Zhang, Y., Wang, Y., & Zhang, T. (2026). Prediction of static liquefaction
1021 landslides in loess: Integrating triaxial shear parameters into the sliding-block model.
1022 Engineering Geology, 108549, 10.1016/j.enggeo.2026.108549.

1023 Zhang, W. M., Qi, J. B., Wan, P., Wang, H. T., Xie, D. H., Wang, X. Y., and Yan, G. J.: An Easy-
1024 to-Use Airborne LiDAR Data Filtering Method Based on Cloth Simulation, Remote Sens,
1025 8, 501, 10.3390/rs8060501, 2016.

1026 Zhu, J. F., Nolte, A. M., Jacobs, N., and Ye, M.: Using machine learning to identify karst
1027 sinkholes from LiDAR-derived topographic depressions in the Bluegrass Region of
1028 Kentucky, J Hydrol, 588, 125049, 10.1016/j.jhydrol.2020.125049, 2020.

1029 Zhu, J. F. and Pierskalla, W. P.: Applying a weighted random forests method to extract karst
1030 sinkholes from LiDAR data, J Hydrol, 533, 343–352, 10.1016/j.jhydrol.2015.12.012, 2016.

1031 Zumpano, V., Pisano, L., and Parise, M.: An integrated framework to identify and analyze karst
1032 sinkholes, Geomorphology, 332, 213–225, 10.1016/j.geomorph.2019.02.013, 2019.